Earth Systems and Environment
https://doi.org/10.1007/s41748-026-01266-5

ORIGINAL ARTICLE

Vertical Distribution of Cloud Area Fraction and Associated Cloud Radiative Effects over East Africa Using MERRA-2 Reanalysis and CERES (2000–2025) Data

Geoffrey W. Khamala[1] · John W. Makokha[2] · Churchill Wanyera[1] · Kanike Raghavendra Kumar[3] · Mansour Almazroui[4,5] · Pelati Althaf[3] · Aqil Tariq[6]

Received: 16 February 2026 / Revised: 14 May 2026 / Accepted: 20 May 2026

Abstract

The Cloud Area Fraction (CAF) and Cloud Radiative Effect (CRE) are among the key metrics for understanding Earth's climate, as they modulate shortwave and longwave radiation. This study, therefore, analyzes the vertical distribution of CAF and their associated CRE over East Africa (EA) using the Modern-Era Retrospective Analysis for Research and Applications Version (MERRA-2) reanalysis and Clouds and the Earth's Radiant Energy System (CERES) observational data from 2000 to 2025. The vertical CAFs for low, middle, and high clouds are computed at pressure levels and spatially averaged over EA. These are used to derive shortwave CRE ($\mathrm{CRE_{SW}}$ in $\mathrm{Wm^{-2}}$), longwave CRE ($\mathrm{CRE_{LW}}$ in $\mathrm{Wm^{-2}}$), and net CRE (in $\mathrm{Wm^{-2}}$) from all-sky and clear-sky radiative fluxes. The validation of MERRA-2 CAF against CERES observations showed it to be reliable (r=0.749), supporting its use for analyzing cloud-radiation patterns, including vertical cloud distribution. The study of vertical CAF and CRE over EA using MERRA-2 reveals a strongly stratified cloud climatology shaped by topography, lake impacts, and large-scale circulation. The vertical CAFs at Low, mid, and high clouds show distinct spatial and temporal patterns, with high clouds intensifying the most with more than 60% of the total CAF ($\sim$0.256), while the contribution of the low CAF against the total covers $\sim$18% ($\sim$0. 076) is the least. Further, the spatiotemporal CRE is dominated by shortwave cooling, ranging from −14.71 to -54.36 W $\mathrm{m^{-2}}$, which moderates regional temperatures. Cloud layers interact to influence rainfall: low clouds enhance local convection, mid clouds regulate moisture transport, and high clouds mark mature convective systems. This collectively reinforces EA's bimodal rainfall pattern and highlights the critical role of clouds in regional climate dynamics. This study recommends future analyses that integrate long-term model outputs with satellite and ground-based observations to validate cloud patterns. Such emphasis should focus on the CREs of low, middle, and high clouds, their links to rainfall, and model uncertainties to improve understanding of the role of cloud dynamics over EA's climate.

✉ Kanike Raghavendra Kumar
kanike.kumar@gmail.com; rkkanike@kluniversity.in

Aqil Tariq
at2139@msstate.edu

[1] Department of Renewable Energy and Technology, Turkana University College, P.O. Box 69-30500, Lodwar, Kenya

[2] Department of Science, Technology, and Engineering, Kibabii University, P.O. Box 1699-50200, Bungoma, Kenya

[3] Department of Engineering Physics, College of Engineering, Koneru Lakshmaiah Education Foundation (KLEF), Vaddeswaram, Guntur 522302, Andhra Pradesh, India

[4] Center of Excellence for Climate Change Research, Department of Meteorology, King Abdulaziz University, Jeddah, Saudi Arabia

[5] Climatic Research Unit, School of Environmental Sciences, University of East Anglia, Norwich NR4 7TJ, UK

[6] Department of Wildlife, Fisheries, and Aquaculture, College of Forest Resources, Mississippi State University, Starkville, Mississippi State 39762-9690, USA

Published online: 15 June 2026

Graphical Abstract

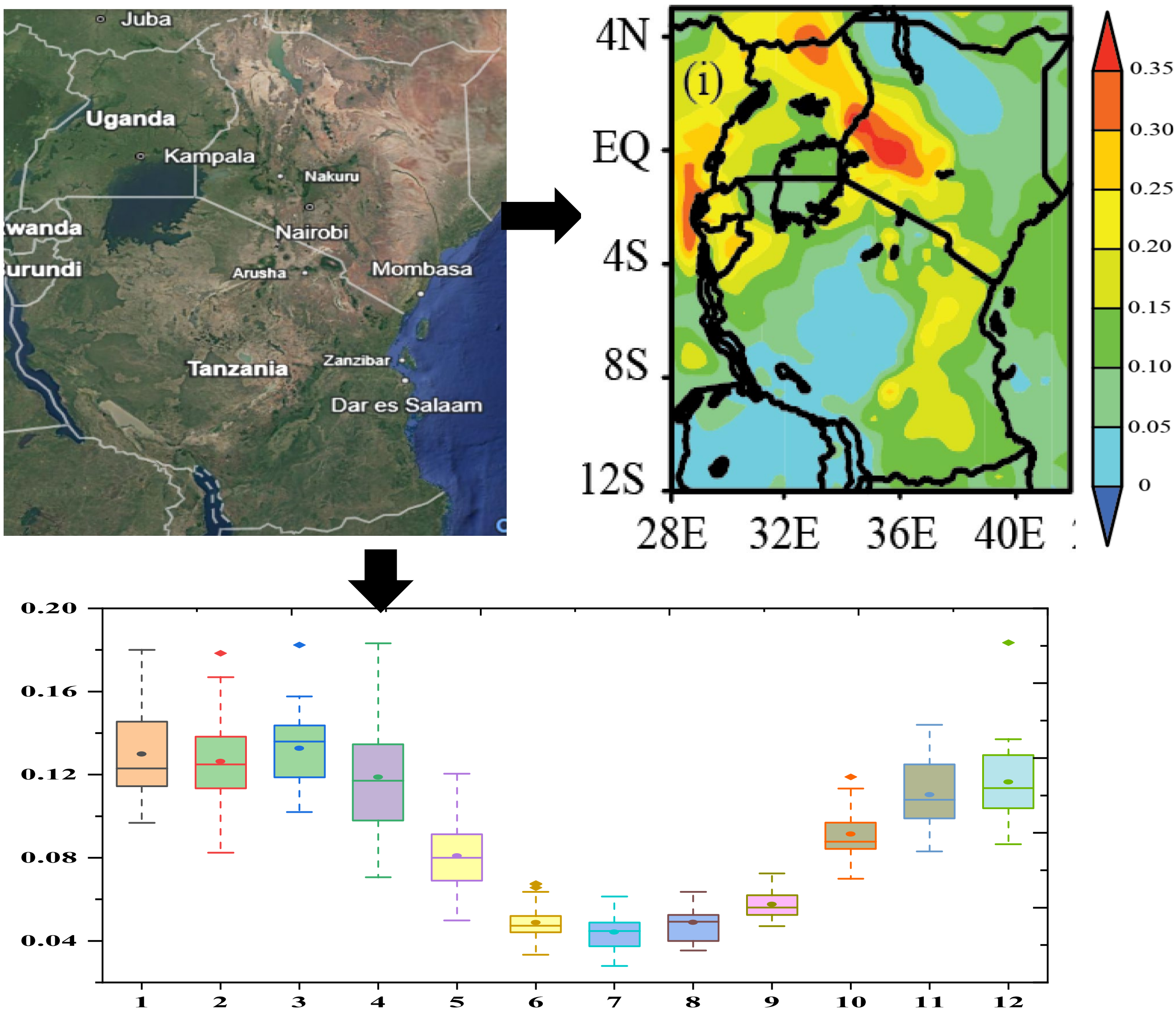

The satellite map of East Africa is presented in the geographical abstract, with key features including Lake Victoria, the highlands of central Kenya and northern Tanzania, and the lowland coastal plains along the Indian Ocean. The graphical abstract highlights that the study focuses on the comprehensive use of MERRA-2 reanalysis and CERES datasets of Cloud Area Fraction (CAF) and Cloud Radiative Effect (CRE) to assess vertical cloud stratification and cloud-radiation interactions over East Africa. The analysis captures both the spatial and temporal evolution of cloud characteristics, recognizing their fundamental role in regulating the Earth's radiation budget through vertical structure and radiative interactions. Spatial patterns reveal marked regional heterogeneity with enhanced cloud coverage over the study region. Further, distinct variations in radiative impacts are observed with cloud altitude, where low-level clouds predominantly contribute to shortwave radiative cooling. In contrast, high-level clouds exhibit a mixed radiative influence due to competing longwave warming and shortwave reflection effects. The analyses and further discussion on cloud-radiation interactions demonstrate pronounced vertical variability in both CAF and CRE, emphasizing the outsized role of high clouds in modulating the regional energy balance.

Highlights

- CAF shows vertically structured variability driven by topography, lake effects, and seasonal ITCZ migration.
- Cloud occurrence increases at all levels, with the strongest intensification in high clouds due to enhanced convection.

- CRE is dominated by shortwave cooling, peaking during convective and rainy seasons across the region.
- Vertical cloud layer interactions influence rainfall variability and help maintain East Africa's characteristic bimodal climate regime.

Keywords Cloud area fraction · Cloud radiative effect · Cloud-precipitation interactions · MERRA-2 · CERES · East Africa

1 Introduction

Clouds are one of the significant fundamental regulators of the Earth's climate system (Balakrishnaiah et al. 2011; Adesina et al. 2016). They exert strong controls on both the shortwave and longwave components of the radiation budget (Kang et al., 2015; Adesina et al., 2016; Makokha et al. 2024; Berhane et al., 2024, 2025), thereby influencing the climate system by reflecting incoming solar radiation to space and by absorbing and re-emitting outgoing surface radiation (Khamala et al. 2023). Further, clouds can cool or warm the surface, depending on their properties and distribution (Ramanathan et al. 1989; Hartmann et al. 1992). The extent to which clouds influence climate depends strongly on altitude, optical thickness, and fractional coverage, which together govern their radiative impacts (Balakrishnaiah et al. 2011; Gopal et al. 2017; Bhavyasree et al. 2024). Because of these complexities, uncertainties in cloud-radiation interactions remain among the key contributors to the spread in estimates of climate sensitivity across global climate models (IPCC, 2021; Berhane et al., 2024, 2025; Althaf et al. 2025; Zelinka et al. 2020; Pan et al. 2024).

Cloud occurrence can be characterized through the Cloud Area Fraction (CAF), defined as the proportion of a given region or grid box covered by clouds. This property provides a key diagnostic for assessing cloud climatology and serves as an input for radiative transfer calculations (Stubenrauch et al. 2013). Notably, CAF varies with altitude: low clouds (below ~2 km) generally increase planetary albedo and exert a cooling influence. In comparison, middle clouds (2–6 km) have mixed radiative effects depending on phase and thickness. On the other hand, the high clouds (above ~6 km) often warm the climate system by trapping longwave radiation while transmitting much of the incoming shortwave radiation (Liou 1986; Rossow and Schiffer 1999). This vertical heterogeneity underscores the need to study CAF within a stratified framework that distinguishes between low, middle, and high clouds.

A closely related effect to the CAF is the Cloud Radiative Effect (CRE), which is the difference between all-sky and clear-sky radiative fluxes and is widely used to quantify the influence of clouds on the Earth's energy budget (Ramanathan et al. 1989). Since CAF affects radiative properties at all wavelengths, CRE can be decomposed into shortwave ($\mathrm{CRE_{SW}}$) and longwave ($\mathrm{CRE_{LW}}$) components, as well as a net component. The strength and sign of CRE are highly altitude dependent, with stratocumulus clouds exerting a strong negative SWCRE while thin cirrus clouds contribute a positive LWCRE (Stephens 2005; Boucher et al. 2013). When studied jointly with CAF, CRE provides a powerful lens for diagnosing how cloud occurrence translates into radiative forcing across atmospheric layers.

Several studies, including observational, satellite, and modeling studies over the past three decades, have significantly advanced the knowledge on CAF and CRE (Ramanathan et al. 1989; Williams and Funk 2011; Balakrishnaiah et al., 2012; Sassen and Wang 2012; King et al. 2013; Stubenrauch et al. 2013; Kang et al. 2015 ; Adesina et al. 2016; Huang et al. 2020; Nyasulu et al. 2020; Dai et al. 2021; Otte et al. 2023; Pan et al. 2024a; Su et al. 2025). Satellite missions such as the Clouds and Earth's Radiant Energy System (CERES), CloudSat, and CALIPSO have provided unprecedented global datasets on cloud area fraction and radiative fluxes (Wielicki et al. 1996; Winker et al. 2010; Pan et al. 2019, 2022; Althaf et al. 2025). These missions have revealed systematic differences among low-, middle-, and high-level clouds in their contributions to CRE. However, satellite records, while invaluable, suffer from relatively short temporal coverage (starting in the early 2000s), sampling biases, and limitations in providing long-term climate diagnostics (Loeb et al. 2018; Liu et al. 2025a, b).

To address the inadequacy in satellite measurements, the reanalysis products address these challenges by assimilating diverse observations into physically consistent numerical weather prediction frameworks. The Modern-Era Retrospective Analysis for Research and Applications, Version 2 (MERRA-2), produced by NASA's Global Modeling and Assimilation Office, for instance, is among the most comprehensive reanalysis datasets available. MERRA-2 spans 1980 to the present and assimilates satellite radiances, in situ observations, and other meteorological data into the GEOS-5 model (Gelaro et al. 2017; Reddy et al. 2021; Bhavyasree et al. 2022). Importantly, it provides all-sky and clear-sky radiative fluxes, allowing direct calculation of CRE, along with vertically resolved cloud-area-fraction diagnostics. This makes it a uniquely suitable dataset for evaluating both CAF and CRE simultaneously over multiple decades.

Recently, several studies have demonstrated the effectiveness of MERRA-2 reanalysis for various research (Giangrande et al. 2017; Khamala et al. 2022, 2023; Althaf et al. 2024; Khamala and Makokha 2025; Berhane et al. 2025). For instance, Giangrande et al. (2017) evaluated MERRA-2 cloud properties against ground-based observations, while Bosilovich et al. (2015) assessed its radiation budget against CERES. Khamala et al. (2023) evaluated the total radiative forcing due to aerosols using the same platform. However, relatively few studies have systematically combined the vertical distribution of CAF with CRE estimates to attribute radiative impacts to specific cloud layers. Yet, such vertically resolved analysis is crucial, as clouds at different levels often exert disproportionate influence on net CRE through their longwave and shortwave effects (Zelinka et al. 2013; B. Pan et al. 2023; Liu et al. 2025a, b). Further, Lubis et al. (2025) showed that cloud radiative effects significantly increase wintertime atmospheric blocking in the Euro-Atlantic sector. Additionally, the results showed that CRE significantly influences large-scale atmospheric circulation. Their study further noted that clouds enhance wave activity and increase the frequency of blocking events in the Euro-Atlantic region.

The present study addresses this gap by explicitly focusing on the vertical distribution of CAF and its associated CRE, derived from MERRA-2 reanalysis and CERES observations over EA. The study partitioned clouds into low (from surface to 680 hPa, corresponding to altitudes below about 2 km), middle (680−440 hPa, 2–6 km), and high (above 440 hPa, higher than 6 km) cloud layers, so that the analysis could provide a vertically resolved understanding of how cloud occurrence modulates radiative fluxes across different atmospheric regimes. The rest of this paper is structured as follows: Sect. 2 illustrates the study area, data, and methodology. Results and discussions are documented in Sect. 3. At the same time, the conclusions and recommendations are summarized, and the key findings from the present work are presented in Sect. 4, which call for future research.

2 Study Region, Meteorology, and Data

2.1 Study Area and Meteorology

The study domain encompasses East Africa, spanning approximately 32°E to 40°E in longitude and 4°S to 12°S in latitude, and includes the countries of Uganda, Kenya, and Tanzania (Fig. 1). The region also transitions from inland continental surfaces to the maritime influence of the western Indian Ocean, creating a complex spatial gradient in temperature, humidity, and boundary-layer dynamics (Boiyo et al. 2017). The study domain, with elevations ranging from a minimum of 4 m above sea level along the Indian Ocean coastline to a maximum of 5,793 m at the summit of Mt. Kilimanjaro in northern Tanzania, represents a total vertical relief of approximately 5,789 m (Fig. 1a). The Shuttle Radar Topography Mission (SRTM) DEM data can be downloaded at the USGS Earth Explorer website (https://earthexplorer.usgs.gov). The dataset represents the topography of the study area at a spatial resolution of 90 m × 90 m. For further details, readers are encouraged to consult Althaf et al. (2024). Low-elevation zones (≤500 m) are predominantly observed along the coastal belt bordering the Indian Ocean and around the arid basin of Lake Turkana in northern Kenya. In contrast, the highest elevations (>4,000 m) are concentrated in isolated volcanic peaks, most notably Mt. Kilimanjaro (5,793 m) and Mt. Elgon (approximately 4,321 m), the latter situated along the Kenya-Uganda border. Intermediate elevations (500-2,500 m) characterize the extensive interior plateaus and the eastern and western rift escarpments that traverse the region. The spatial distribution of elevation classes reveals a steep gradient from the Indian Ocean lowlands westward toward the East African Rift System, with secondary orographic highs associated with Mt. Elgon and Mt. Kilimanjaro (Fig. 1b). These topographic features are expected to exert strong controls on local precipitation patterns, temperature lapse rates, and ecological zonation, thereby influencing hydrological connectivity, agricultural suitability, and biodiversity distribution across the study domain.

Figure 1c presents the mean meteorological conditions at the pressure level of 1000 hPa over East Africa. The Meteorological data (Temperature, Relative humidity, U-component (Zonal), and V-component (Meridional) winds at a pressure level of 1000 hpa) was retrieved from Copernicus Europe's Eyes on Earth portal, as implemented by the ECMWF (https://climate.copernicus.eu/climate-reanalysis). This dataset provides atmospheric parameters at a standard resolution of 0.25° x 0.25° for 37 pressure levels from 1979 to three months post-real-time (Althaf et al. 2024). The color-filled contours represent mean air temperature in Kelvin (K), the red solid contour lines indicate relative humidity in percent (%), and the arrows denote wind vectors, where arrow length corresponds to wind speed and arrow orientation indicates wind direction. The mean temperatures at 1000 hPa range from approximately 295 K over the southern highlands of Tanzania to more than 305 K across the low-lying arid regions of northern Kenya and near Lake Turkana. A pronounced thermal gradient is observed between the warmer Indian Ocean coastline (exceeding 303 K) and the relatively cooler interior rift valley, particularly over Uganda and western Kenya, where elevations are higher. The low temperatures within the domain are recorded near Mt. Kilimanjaro and

Mt. Elgon, reflecting the localized orographic cooling effect even at this lower atmospheric level.

Relative humidity values, shown by the red grid lines, range from below 30% over the dry northeastern sector of the domain (northern Kenya) to above 80% along the Indian Ocean coast and over Lake Victoria. A strong east-west moisture gradient is evident, with relative humidity exceeding 70% over Uganda and western Tanzania, decreasing sharply to less than 50% east of 38°E. This pattern is primarily attributed to moisture advection from the Atlantic and Congo Basin, combined with local evapotranspiration from large lake surfaces. The wind field at 1000 hPa reveals a dominant southeasterly flow south of the equator (approximately 6°S to 12°S), veering to easterly or northeasterly north of the equator (3°N to 3°S). Wind speeds, represented by arrow length, are strongest (estimated at 8–10 m/s) across the Turkana Channel in northern Kenya and over the Indian Ocean offshore of Tanzania, where the southeasterly trade winds are accelerated by topographic funneling and regional pressure gradients. Conversely, wind speeds are weakest (below 2–3 m/s) over the Lake Victoria basin and the Rwenzori region along the Uganda-DRC border, where local convergence and frictional orographic effects dominate.

The confluence of warm temperatures exceeding 303 K, moderate relative humidity between 50% and 70%, and converging easterly and southeasterly winds along the equatorial band (3°S to 3°N) delineates the core of the Intertropical Convergence Zone (ITCZ) at the 1000 hPa level, indicating enhanced convective potential. In contrast, the hot (> 305 K), dry (< 40% RH), and strongly advective environment over the Turkana low-level jet corridor represents a major moisture-divergence zone, explaining the persistent aridity of northern Kenya even during peak monsoon seasons.

The region experiences a tropical climate, with the seasonal migration of the ITCZ driving a bimodal rainfall pattern across much of the area (Ongoma and Chen

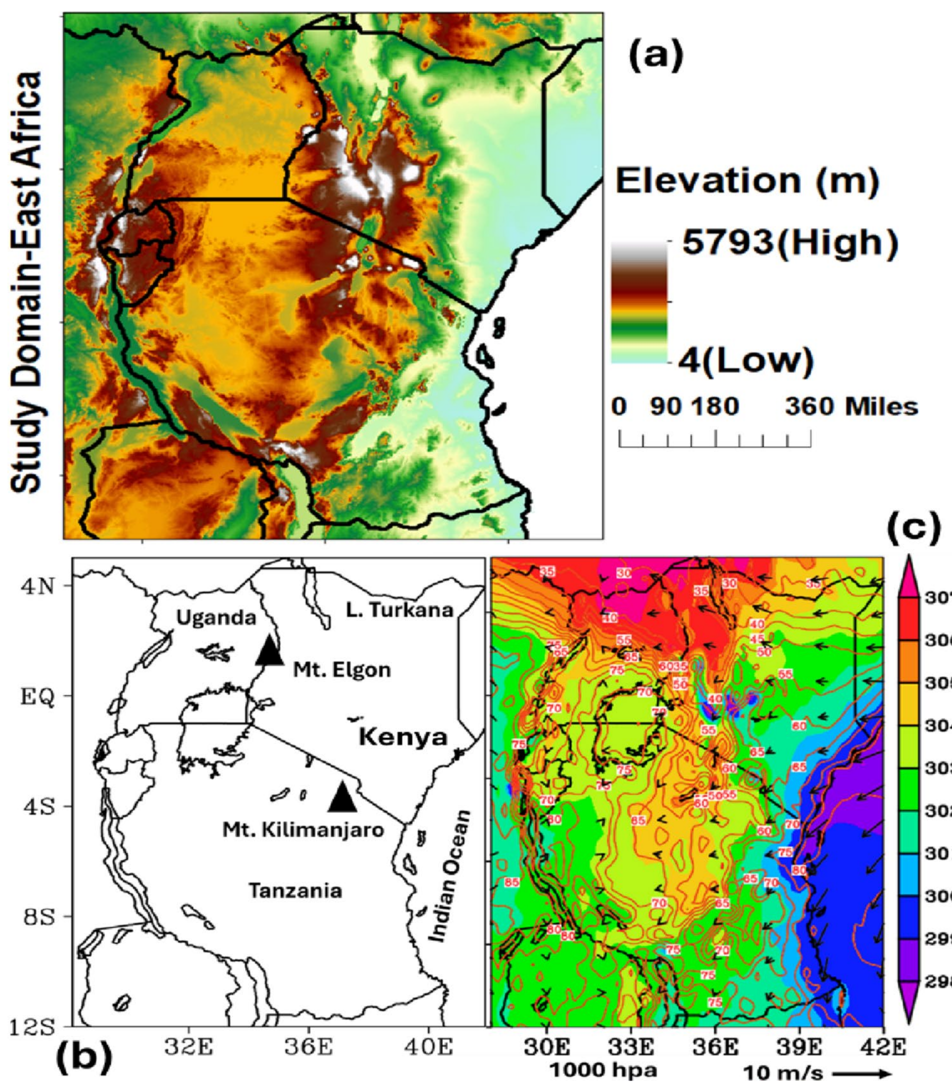

Fig. 1 (**a**) Topography map of East Africa, and the corresponding color scale represents the elevation or altitude in meters (m). (**b**) The study domain covers the East African region, including Uganda, Kenya, and Tanzania, and illustrates the geographical extent of these countries, along with key physiographic features relevant to the analysis. Major topographic landmarks are highlighted, including Mt. Elgon along the Kenya-Uganda border and Mt. Kilimanjaro in northern Tanzania. (**c**) The annual mean synoptic meteorological parameters of wind speed (in m/s), wind direction (in deg), air temperature (in K), and relative humidity (in %) were derived at 1000 hPa. The colored scale with the contour represents the mean air temperature, red solid grid lines represent the relative humidity, the length of black-colored arrows represents the magnitude of wind speed, and the direction of the arrow indicates the wind direction

2017; Boiyo et al. 2018; Aklesso et al. 2018; Khamala et al. 2022). Based on prevailing meteorological conditions, the region has four seasons, i.e., January-February (JF) and June-July-August-September (JJAS) represent the local dry seasons, characterized by reduced rainfall and increased aerosol load. On the other hand, March-April-May (MAM) and October-November-December (OND) represent the local wet seasons, characterized by enhanced rainfall and reduced aerosol concentrations (Ayugi et al. 2016; Nicholson 2017; Gebrechorkos et al. 2019; Caroline et al. 2021). Further, the moisture influx from the Indian Ocean, combined with orographic lifting over major mountain ranges, enhances convective activity and modulates cloud vertical structure. The domain is also influenced by lake–breeze circulations, particularly around Lake Victoria and Lake Turkana, which contribute to localized convection and diurnal cloud variability.

2.2 Instrumentation and Satellite Data

This study utilizes cloud and radiation products derived from the MERRA-2 reanalysis and CERES satellite data. The MERRA-2 model is a state-of-the-art atmospheric reanalysis dataset produced by NASA's Global Modeling and Assimilation Office (GMAO) (Rienecker et al. 2011; Gelaro et al. 2017; Khan et al. 2021; Reddy et al. 2021; Khamala et al. 2022, 2024; Bhavyasree et al. 2022; Khamala and Makokha 2025; Simiyu et al. 2025). This platform provides a consistent long-term record of atmospheric variables by assimilating a wide range of satellite and in situ observations into the GEOS-5 atmospheric model using an advanced data assimilation system (Rienecker et al. 2011; Khan et al. 2021). The dataset offers high temporal resolution at a spatial resolution of $0.5° \times 0.625°$, making it suitable for regional-scale analyses. This model performs meteorological data assimilation, aerosols analysis, precipitation, water vapor climatology, and temperature using NASA's observations of stratospheric ozone. Building on the success of the atmospheric reanalysis conducted with GEOS, the MERRA-2 model intends to produce a major Earth System Reanalysis of the atmosphere, land, ocean, and ice at a latitude-longitude grid. In the present study, MERRA-2 M2TMNXRAD_5_12_4 for low (from surface to 680 hPa, corresponding to altitudes below about 2 km), middle (680−440 hPa, 2–6 km), and high clouds (above 440 hPa, higher than 6 km) were retrieved to analyze spatiotemporal trends in cloud products. These data products were sourced from http://giovanni.gsfc.nasa.gov/giovanni/.

CERES is a satellite instrument developed by NASA to measure the Earth's radiation budget with high accuracy (Wielicki et al. 1996; Loeb et al. 2018). CERES instruments are deployed on several Earth-observing satellites, including Terra, Aqua, and Suomi NPP, providing continuous, global measurements of radiative fluxes at multiple levels: the top of the atmosphere (TOA), within the atmosphere, and at the Earth's surface. These measurements cover both shortwave (solar) and longwave (thermal infrared) radiation, key for quantifying the Earth's energy balance and understanding climate processes. Further, the platform measures shortwave radiation in the spectral range from 0.3 µm to 5 µm, which includes visible and near-infrared wavelengths where solar radiation is most intense. It also measures longwave radiation in the thermal infrared range, between 8 μm and 12 µm, capturing the Earth's emitted heat energy. It can distinguish between the effects of reflected solar radiation and emitted terrestrial radiation, enabling detailed analyses of CRE. The CERES EBAF (Energy Balanced and Filled) Fluxes and CLOUD_AMT CERES SYN1deg Cloud Amount (%) used were sourced from the NASA/POWER Source Native at a monthly temporal resolution and spatial resolution of $0.5° \times 0.625°$.

However, before analyzing the vertical cloud distribution and its associated CRE, the reanalysis datasets needed to be validated. The study, therefore, validated the total CAF from MERRA-2 against the total cloud from CERES to ensure a consistent comparison of column-integrated cloud properties. Figure 2 presents a validation scatter plot comparing total MERRA-2 CAF and CERES total cloud data. The validation ensured that the modeled metrics are reliable and physically meaningful, as they integrate observational data with numerical models, but they may exhibit bias due to model assumptions, parameterizations, or spatial and temporal limitations. Once validated, MERRA-2 data were used confidently to infer both vertical and spatial cloud-radiation patterns.

The results in Fig. 2 indicate a good correlation between MERRA-2 and the CERES cloud amount data. The Pearson correlation coefficient ($r = 0.749$) indicates a clear relationship: an increase in MERRA-2 CAF is associated with a corresponding increase in CERES cloud amount. This level of consistency provides confidence that the reanalysis product is physically meaningful and not random with respect to observations. Given this statistically significant correlation, MERRA-2 CAF can be considered sufficiently reliable for further analysis in this study, particularly for examining aspects not directly available from CERES, such as the vertical distribution of clouds.

3 Methodology

The study is designed to evaluate the vertical distribution of CAF using the MERRA-2 modeled data. The analysis covers low-, mid-, and high-level clouds to quantify their climatology, variability, and spatial patterns over EA. The cloud layer thresholds were classified based on cloud top pressure (CTP) where low clouds (CTP>680 hPa), middle clouds (CTP between 440 and 680 hPa), and high clouds (CTP<440 hPa). The CAF at each vertical level is computed by summing the cloud fractional coverage across all grid cells within the corresponding pressure layer, yielding the total cloud fraction for that layer.

Suppose $f(p,t,x,y)$ denote the cloud area fraction (CAF) at the pressure level p, time t and location (x,y), then the mean CAF for a given layer L (low, mid, or high) is given by Eq. 1.

$$\mathrm{CAF_L}(t,x,y) = \frac{1}{N_L}\sum_{p=L} f(p,t,x,y) \tag{1}$$

where $\mathrm{CAF_L}$(x, y,t) is a spatially varying quantity (e.g., a field value at position $(x,y)$and time t) and N_L is the number of pressure levels included in the layer L.

The regional mean CAF over the study domain was obtained by spatially averaging across grid cells. For the CAF calculation, the layer-specific averaged values across pressure levels were weighted to reduce the local-scale variability and large-scale cloud distribution patterns, enhancing direct comparison with observational benchmarks. To derive the large-scale means, the CAF values were aggregated across vertical bands corresponding to the low, mid and high clouds. Since the geometry of the earth introduces unequal weighting of grid cells by latitude, the average over the study domain was calculated using cosine-latitude $(\theta$) weighting given as in Eq. 2, ensuring that all regions are proportionally represented in the climatological means on the grid and spatial resolution.

$$\overline{CAF_L(t)} = \frac{\sum_{x,y} \mathrm{CAF_L}(x,y,t)\cdot\cos\theta}{\sum_{x,y}\cos\theta} \tag{2}$$

where $\mathrm{CAF_L}$(x, y,t) is a spatially varying quantity (e.g., a field value at position $(x,y)$and time t), θ is typically an angle associated with each (x,y)point (often related to orientation or direction), and cosθ is a weighting factor.

Grid-wise linear regression trends in CAF were evaluated using the merged monthly time-area-averaged dataset from 2000 to 2025. The approach reviewed by Weatherhead et al. (1998) and utilized in numerous correlated research studies (Kumar et al. 2015; Boiyo et al. 2018; Hu et al. 2018; Khamala et al. 2022; Althaf et al. 2024) has the advantage of simply assessing the direction and magnitude of variations in long-term data. Incidentally, the simple linear trend model (Eq. 3) was adopted by the current study. i.e.

$$Y_t = aX_t + b + N_t,\ t = 1,\ldots\ldots,T \tag{3}$$

where Y_t is a geophysical variable, whose trend is being determined (CAF at low, middle and high levels), b offset (y-intercept) that denotes the value of Y_t at the start of the time series. X_t is an independent variable indicating a time series ($X_t = \frac{t}{12}$, where t is a specific month in a time series, a is the assessed trend in a geophysical variable under consideration, while N_t is noise in a time series. Significance in assessed trends was analyzed in Eq. 4.

$$\delta = \frac{\sigma_N}{n^{3/2}}\sqrt{\frac{1+\Phi}{1-\Phi}} \tag{4}$$

The trends are deemed significant at a p-value of 0.05 or a 95% confidence level when $\left|\frac{\omega}{\delta}\right| \geq 2$ while trends are regarded as significant at 90% confidence level when $1.5 \leq \left|\frac{\omega}{\delta}\right| < 2$, where is the standard deviation of the slope ω gotten from linear regression (Weatherhead et al. 1998; Khamala et al. 2022).

To determine the CRE, the difference between all-sky (with cloud) and clear-sky (without cloud) radiative fluxes was achieved using Eq. 5.

$$\mathrm{CRE} = R_{all} - R_{clear} \tag{5}$$

where R_{clear} is the clear-sky radiation flux while R_{All} is the all-sky radiation flux is given by Eq. 6

$$R = SW_{\downarrow} - SW_{\uparrow}) + LW_{\downarrow} - LW_{\uparrow}) \tag{6}$$

To obtain the CRE in Eq. 5, the time step and grid cell CRE were computed using Eqs. 7, 8, and 9, which separated it into shortwave (top of the atmosphere) and longwave (bottom of the atmosphere) components.

$$\begin{aligned}\mathrm{CRE_{SW}}(t,x,y) &= (SW_{\downarrow} - SW_{\uparrow})^{all}(t,x,y)\\ &\quad - (SW_{\downarrow} - SW_{\uparrow})^{clear}(t,x,y)\end{aligned} \tag{7}$$

where $\mathrm{CRE_{SW}}(t,x,y)$ is a Shortwave Cloud Radiative Effect at time t and horizontal location (x,y) , $(SW_{\downarrow} - SW_{\uparrow})^{all}(t,x,y)$ is Shortwave radiation under all-sky conditions (includes clouds), and $(SW_{\downarrow} - SW_{\uparrow})^{clear}(t,x,y)$ is Shortwave radiation under clear-sky conditions (no clouds).

$$\begin{aligned}\mathrm{CRE_{LW}}(t,x,y) &= (LW_{\downarrow} - LW_{\uparrow})^{all}(t,x,y)\\ &\quad - (LW_{\downarrow} - LW_{\uparrow})^{clear}(t,x,y)\end{aligned} \tag{8}$$

Where $\mathrm{CRE_{LW}}(t,x,y)$ is Longwave Cloud Radiative Effect.

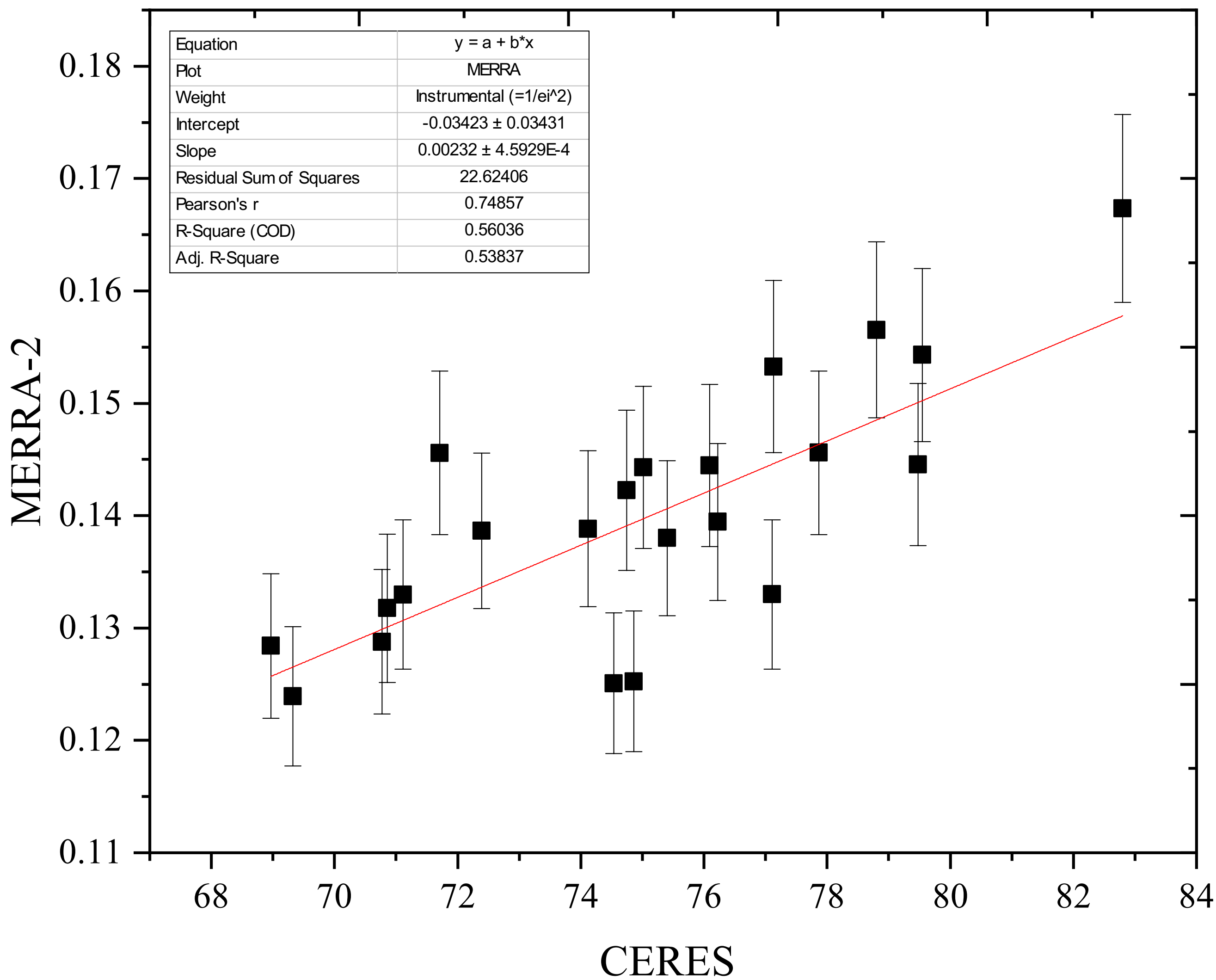

Fig. 2 Validation of MERRA-2 against CERES cloud data. The scatterplot with error bars shows the relationship between the two datasets, with the red line representing the linear regression fit. The Pearson correlation coefficient (r=0.749) suggests a good agreement

(effect of clouds on outgoing longwave/infrared radiation) at time t, horizontal location (x, y), and vertical level z, $(\mathrm{LW}_{\downarrow} - \mathrm{LW}_{\uparrow})^{\mathrm{all}}(\mathrm{t,x,y})$ is Longwave radiation under all-sky conditions (with clouds), and $(\mathrm{LW}_{\downarrow} - \mathrm{LW}_{\uparrow})^{\mathrm{clear}}(\mathrm{t,x,y})$ is Longwave radiation under clear-sky conditions (no clouds).

$$\mathrm{CRE}_{\mathrm{net}} = \mathrm{CRE}_{\mathrm{SW}}\,(\mathrm{t,x,y}) + \mathrm{CRE}_{\mathrm{LW}}\,(\mathrm{t,x,y}) \tag{9}$$

The CRE_{net} is the difference between the radiative flux with clouds (all-sky) and the radiative flux in the same atmospheric state but without clouds (clear sky). $CRE_{SW}\,(\mathrm{t,x,y}) + CRE_{LW}$ is negative since clouds reflect solar radiation, causing a cooling effect, while $CRE_{LW}\,(\mathrm{t,x,y})$ traps outgoing longwave radiation, thereby causing a warming effect.

From the net CRE defined in Eq. 8, the CRE at the top of the atmosphere was determined using equations' 10 and 11 as:

$$\mathrm{CRE}_{\mathrm{SW}}^{\mathrm{TOA}} = \mathrm{SW}_{\uparrow}^{\mathrm{all}} - \mathrm{SW}_{\uparrow}^{\mathrm{clear}} \tag{10}$$

$$\mathrm{CRE}_{\mathrm{LW}}^{\mathrm{TOA}} = \mathrm{LW}_{\uparrow}^{\mathrm{all}} - \mathrm{LW}_{\uparrow}^{\mathrm{clear}} \tag{11}$$

4 Results and Discussion

4.1 Spatial Analysis of Cloud Area Fraction

4.1.1 Low-Level Cloud Area Fraction

Figure 3 illustrates the spatial distribution of low-altitude clouds over the EA region, revealing heterogeneity across the region in most months. To start, the areas around Lake Victoria, northern Tanzania, and western Kenya exhibit higher cloud fraction (>0.25) throughout the year. The enhanced cloud area fraction all year round is probably linked to land-lake interactions, moisture convergence, and convective uplift due to localized circulation driven by the lake's thermal contrast (Anyah et al. 2006; Sun et al. 2019) as indicated in Sect. 2.1.

Further, the elevated cloud cover along the western highlands of Kenya and Uganda corresponds to orographic forcing induced by the Rift Valley escarpments and surrounding elevated terrain (Yang et al. 2015). Notably, during the local wet months (MAM and OND), the equatorial zone demonstrates a North-South oscillation of cloud maxima, corresponding to the seasonal migration of ITCZ, governing the timing and intensity of the bimodal rainfall pattern over the region (Camberlin and Philippon 2002; Dunning et al. 2016; Aklesso et al. 2018).

Conversely, the region in Eastern Kenya and Southern Tanzania experiences reduced low-level cloud, with values < 0.10, as highlighted in Fig. 3. These areas are influenced by subsiding dry air masses associated with the descending branch of the Hadley circulation and by the advection of warm, dry air from the Indian Ocean, particularly during boreal winter (Nicholson 2017). Such conditions suppress cloud formation, consistent with the arid-to-semiarid climates of these regions. However, during the JJAS, the low cloud area fraction is high (> 0.3) mainly due to cool, stable atmospheric conditions associated with the southeast monsoon, which flows from the Indian Ocean. As a result, the moist maritime air moves inland and is trapped beneath temperature inversions, especially over elevated terrain and near large bodies of water. This further reduces convection and strong subsidence associated with the subtropical high, suppressing deep cloud formation and favoring widespread low-level clouds despite limited rainfall.

4.1.2 Mid-Level Cloud Area Fraction

The spatial pattern of mid-level (680 − 440 hPa) CAF across East Africa is characterized by elevated cloud area fractions (>0.25) over the western Rift and highland sectors (Fig. 4). Given the higher mid CAF observed in the region, this study attributed it to persistent uplift and effective moisture convergence. This offsets any suppression in mid-level cloud formation induced by warming. On the other hand, values below 0.05 are observed in mid CAF across the eastern, coastal, and southern regions of the study domain. These low values in the mid CAF have significant implications, as they are not only a function of local orographic forcing and moisture supply but also of large-scale circulation and thermodynamic conditions, which themselves are subject to change under a warming climate. For instance, global and regional analyses by Mendoza et al. (2021) indicate that increasing mid-tropospheric temperatures tend to reduce cloud cover when relative humidity decreases or remains constant.

4.1.3 High-Level Cloud Area Fraction

The spatial distribution of high-level CAF over EA exhibits pronounced latitudinal and regional gradients (Fig. 5), which reflect the influence of large-scale circulation, topography, and moisture transport. In the northern sector, particularly around northern Uganda, high-level clouds are more prevalent, with CAF values frequently exceeding > 0.6. This enhanced cloudiness is consistent with the region's proximity to the tropical convection core and the seasonal migration of the ITCZ, which promotes deep convective development and the formation of extensive clouds (Nicholson 2018; Williams and Funk 2011).

Moving southward toward Tanzania, there is a progressive decline in high-level CAF, with values decreasing to 0.3–0.5 across most of the southern domain. This spatial transition corresponds with reduced convective intensity and lower tropospheric moisture content relative to equatorial latitudes. The Congo Air Boundary and associated westerly moisture influx weaken in the subtropics, resulting in less frequent deep convection and fewer high altitude cloud anvils (Munday et al. 2021). Coastal regions along the western Indian Ocean exhibit moderate to high-level cloud cover, influenced by onshore moisture transport and occasional convection associated with the East African monsoon regime. The maxima cloud cover appears in western Kenya and the Lake Victoria basin, where mesoscale circulations, particularly lake-land breeze interactions, support frequent deep convective storms capable of generating high-level clouds (Tierney et al. 2015).

4.2 Temporal Variability of Cloud Area Fraction

4.2.1 Low-Level Cloud Area Fraction

The monthly variations in cloud area fraction over EA, as shown in Fig. 6, reveal distinct and systematic patterns across the low-level clouds that are closely linked to the

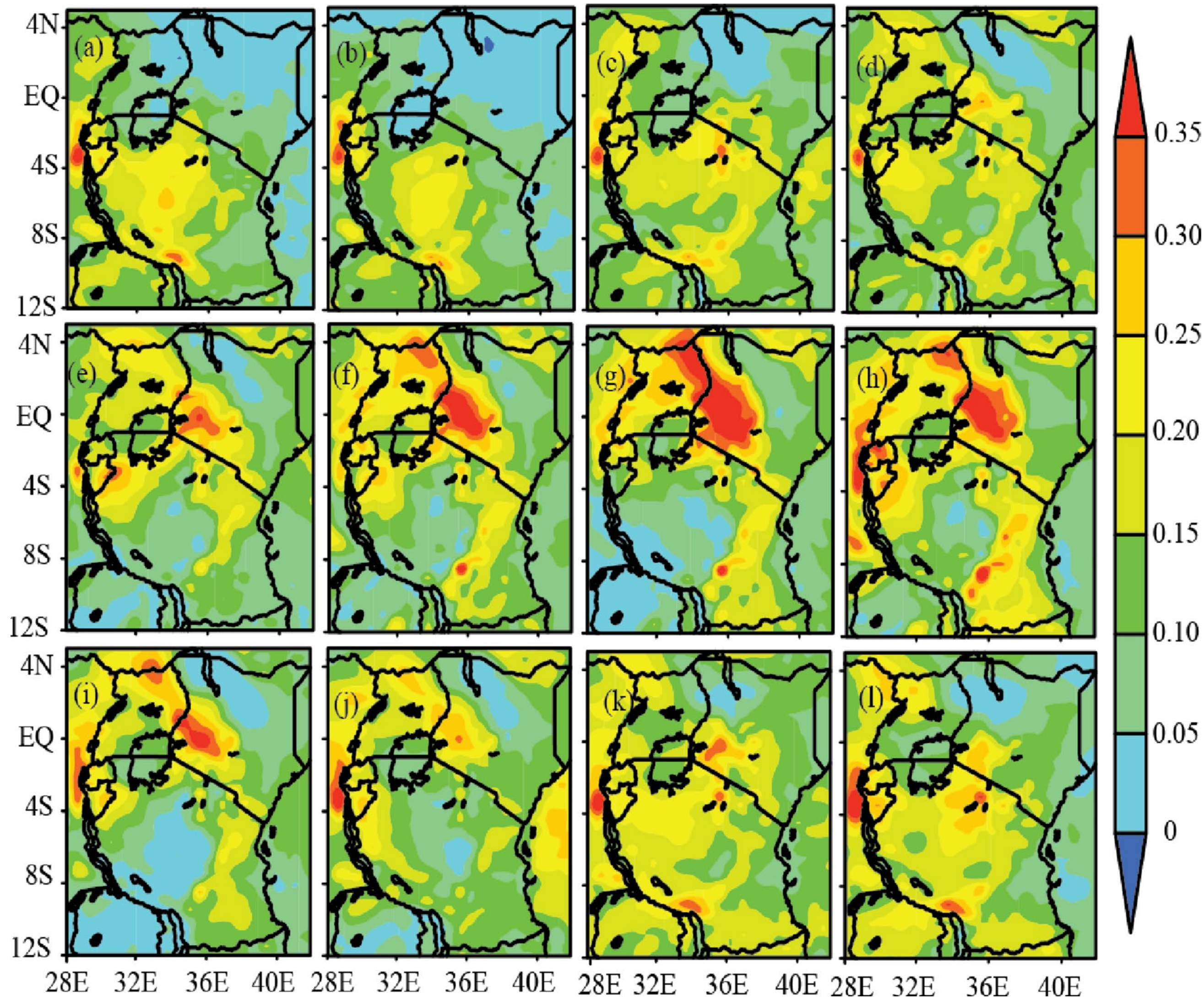

Fig. 3 Spatial distribution of low-level (from surface to 680 hPa) cloud area fraction (CAF) over the study domain for each month. Panels (**a**) through (**l**) represent monthly distributions starting from January (**a**) to December (**l**). The color bar on the right indicates the CAF of low-lying clouds

seasonal migration of the ITCZ, regional circulation systems, and surface thermodynamic conditions. First, in panel (a) (Fig. 6a), the low-level CAF exhibits a pronounced seasonal cycle modulated by regional circulation dynamics, surface temperature gradients, and moisture availability. The lowest mean cloud area fractions of ∼0.35 to ∼0.40 occur during JF, coinciding with the local dry season. This is attributed to strong solar heating, limited surface moisture, and suppressed cloud formation, which are enhanced. This period precedes the MAM season, which records the lowest mean CAF of ∼ 0.33 in March.

During April and May, the low-level CAF gradually increases to about 0.42–0.45, reflecting enhanced boundary-layer moisture and convective mixing associated with the arrival of the ITCZ and the intensification of moist westerly flows from the Congo Basin (Camberlin and Philippon 2002; Nicholson 2017). While in JJAS, there is a notable increase in low-level clouds exceeding 0.50, with a peak in August. This maximum CAF occurs during the dry season over much of EA when the ITCZ shifts northward. Despite limited rainfall, the elevated low-level CAF is attributed to strong temperature inversions, cold advection from the Indian Ocean, and marine boundary layer clouds that develop under stable atmospheric conditions (Mutemi 2003; B. Pan et al. 2023). The Coastal and highland regions often experience extensive morning low clouds and fog,

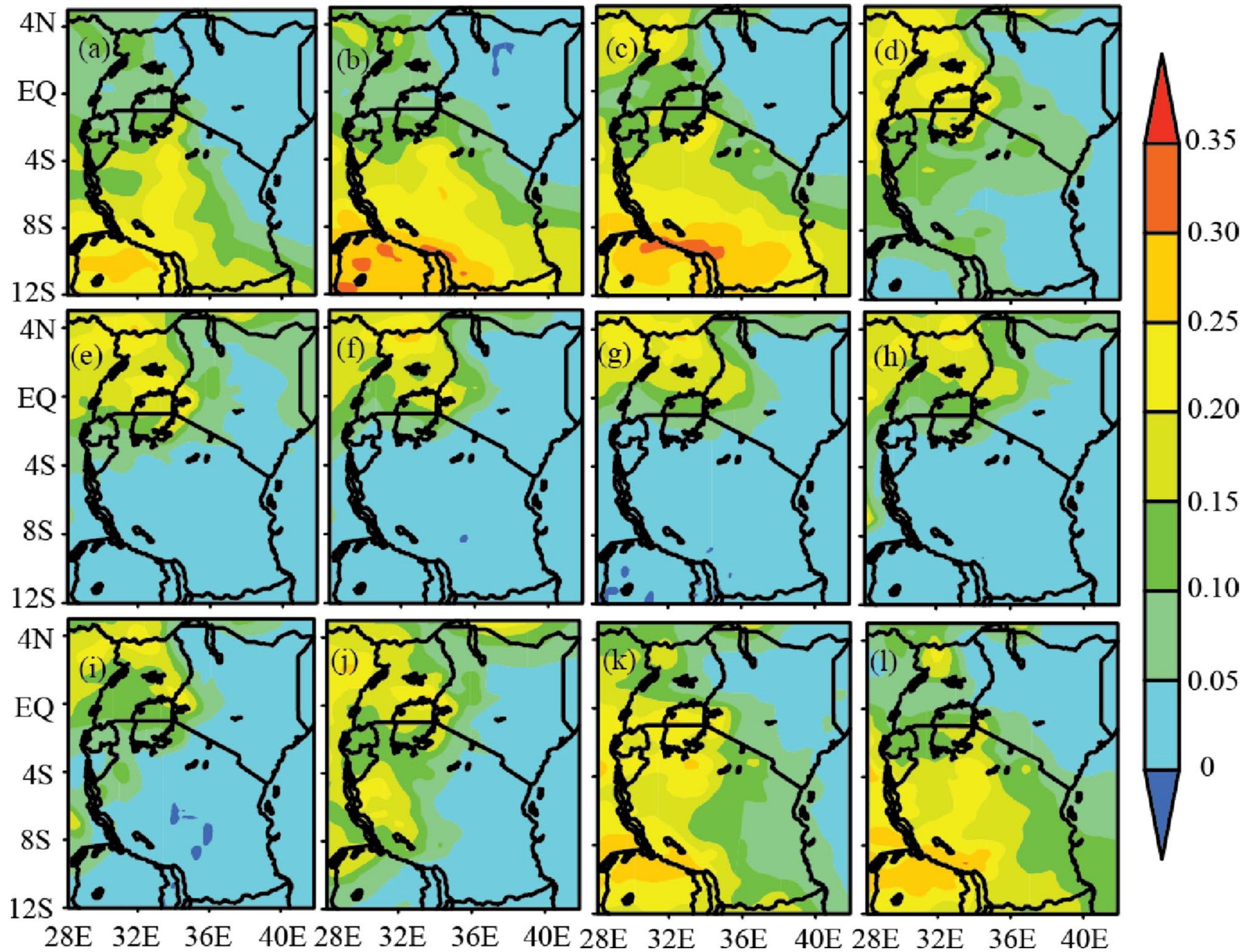

Fig. 4 Spatial distribution of middle-level (680 − 440 hPa) cloud area fraction (CAF) over the study domain for each month. Panels (**a**) through (**l**) represent monthly distributions starting from January (**a**) to December (**l**). The color bar on the right indicates the CAF of middle-lying clouds

contributing to this elevated fraction (Okoola 1996). Thereafter, the low-level CAF decreases from about 0.48 to 0.40 during the OND season. This is attributed to enhanced convection and vertical mixing that erode low-level inversions, favoring the formation of deeper convective clouds (Nicholson 2018; Segele et al. 2015).

Table 1 shows the monthly variation in the low-level CAF, averaged over the study domain. Notably, the low-level CAF exhibits relatively stable coverage, with a mean monthly CAF ranging from 0.115 ± 0.015 in February to 0.154 ± 0.007 in November, yielding an annual mean of 0.136 ± 0.054. These values reflect the persistence of low-level CAFs within the boundary layer. The highest coverage in November (0.154 ± 0.007) corresponds to the short rain season, when enhanced surface heating, humidity, and weak inversion layers promote this type of cloud formation. Conversely, the low values of CAFs in February (0.115 ± 0.015) occur during the late dry season, when the atmosphere is drier and more stable (Nicholson 2018).

4.2.2 Mid-Level Cloud Area Fraction

Figure 6b shows that the mid-level CAF also varies seasonally, reflecting alternating wet and dry phases that are influenced by ITCZ and regional circulation patterns (Nicholson 2017). Higher cloud area fractions dominate the MAM and OND periods, while the lowest values occur during JJAS. The mean mid-level CAF peaks $\sim$0.55 in April, coinciding with the long rains season and enhanced convective activity associated with the presence of the ITCZ and moisture influx from the Indian Ocean (Camberlin and Philippon 2002). A secondary maximum of $\sim$0.48 appears in November, consistent with the short rains that accompany the southward return of the ITCZ and increased regional convergence (Nicholson 2018). In contrast, the mid-level cloud area fraction declines markedly during JJAS, reaching minimum mean values of $\sim$0.15 in July, coinciding with the dry season over much of Kenya and northern Tanzania. This reduction reveals strong subsidence linked to the southern

Fig. 5 Spatial distribution of high-level (above 440 hPa) cloud area fraction (CAF) over the study domain for each month. Panels (**a**) through (**l**) represent monthly distributions starting from January (**a**) to December (**l**). The color bar on the right indicates the CAF of high-lying clouds

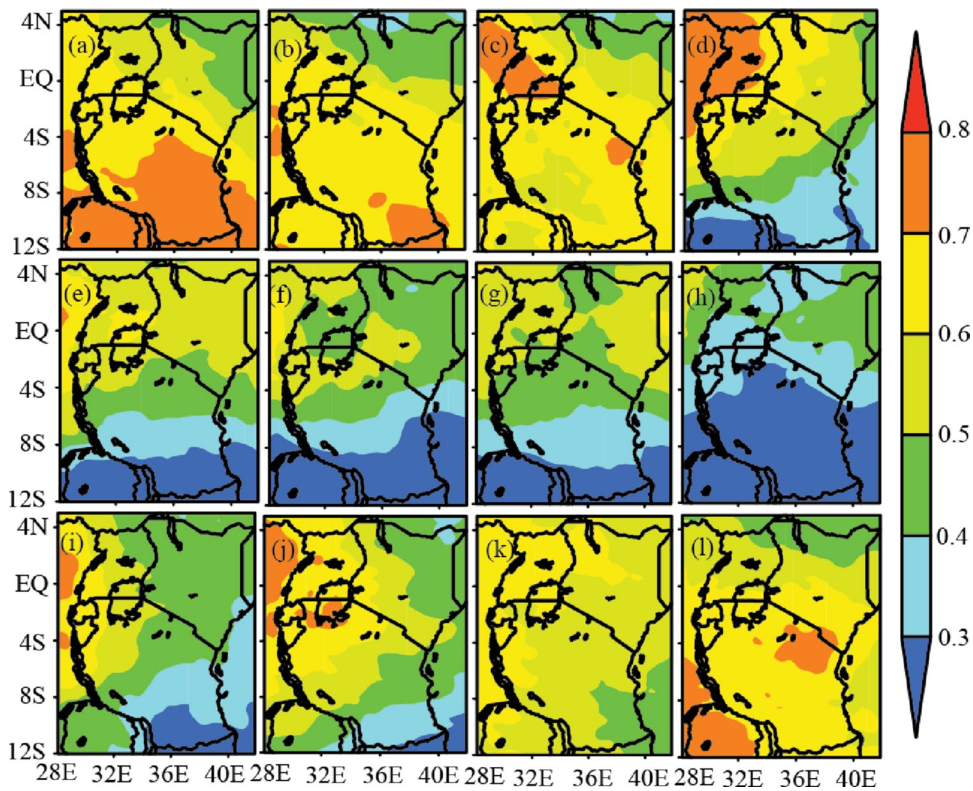

Hadley cell, which suppresses convection and limits cloud formation in the mid troposphere (Anyah and Semazzi 2004). During the JF transition months, the mean CAF of ~ 0.35–0.40 persist, representing residual convection and moisture advection before the onset of rains. Notably, the largest interannual variability occurs in April and November, implying a sensitivity of mid-level cloud formation to large-scale climatic oscillations such as ENSO and the Indian Ocean Dipole (Black et al. 2003; Vigaud et al. 2009).

Further, Table 1 shows that mid-level clouds exhibit lower CAF, with an annual mean of 0.092 ± 0.035, and their distribution closely follows the annual migration of the ITCZ. The CAF peaks in March (0.133 ± 0.019) during the onset of the long rains and drops sharply to the minimum of 0.044 ± 0.009 in July, when subsidence dominates the mid-troposphere. The annual mean in the mid CAF (0.092 ± 0.035) indicates the lowest of the three levels over the study domain.

4.2.3 High-Level Cloud Area Fraction

The high-level CAF (Fig. 6c) follows a distinct bimodal pattern corresponding to the region's rainfall and convective activity cycles. The fraction is highest during MAM and OND, in phase with the long and short rains seasons, respectively. This enhancement in high-level clouds is primarily associated with deep convective systems generated by the ITCZ as it migrates northward and southward across the equator (Nicholson 2018; Williams et al. 2015). However, during the JF period, the mean high-level cloud area fraction remains moderate (~0.65), reflecting a phase of weakened convection following the OND rains. A gradual increase begins in March, culminating in a peak around April, indicating vigorous convection and cloud-top development that favor cloud formation (Okoola 1996). In contrast, a pronounced decline occurs during JJAS, reaching a minimum of ~0.38 in August, consistent with the dry season when the ITCZ has shifted northward, and subsidence dominates the atmospheric column (Mutemi 2003; Nicholson 2017). These stable conditions limit vertical cloud growth and favor clear skies, although low-level clouds persist in coastal and highland areas. Subsequently, during the OND season, a secondary increase occurs, with the high-level cloud area fraction peaking again at ~0.65 in December as the ITCZ returns southward, re-establishing convective uplift and high cloud development (Camberlin and Philippon 2002; Nicholson 2018).

Temporal variation for High-level CAF has been further analyzed in Table 1, and, notably, the values of high CAF are the most extensive, with an annual mean CAF of 0.522 ± 0.110, reflecting their dominance in East Africa's convective cloud systems. The highest values appear in February (0.658 ± 0.044) and March (0.650 ± 0.030), which aligns with the strong convective activity and deep cloud

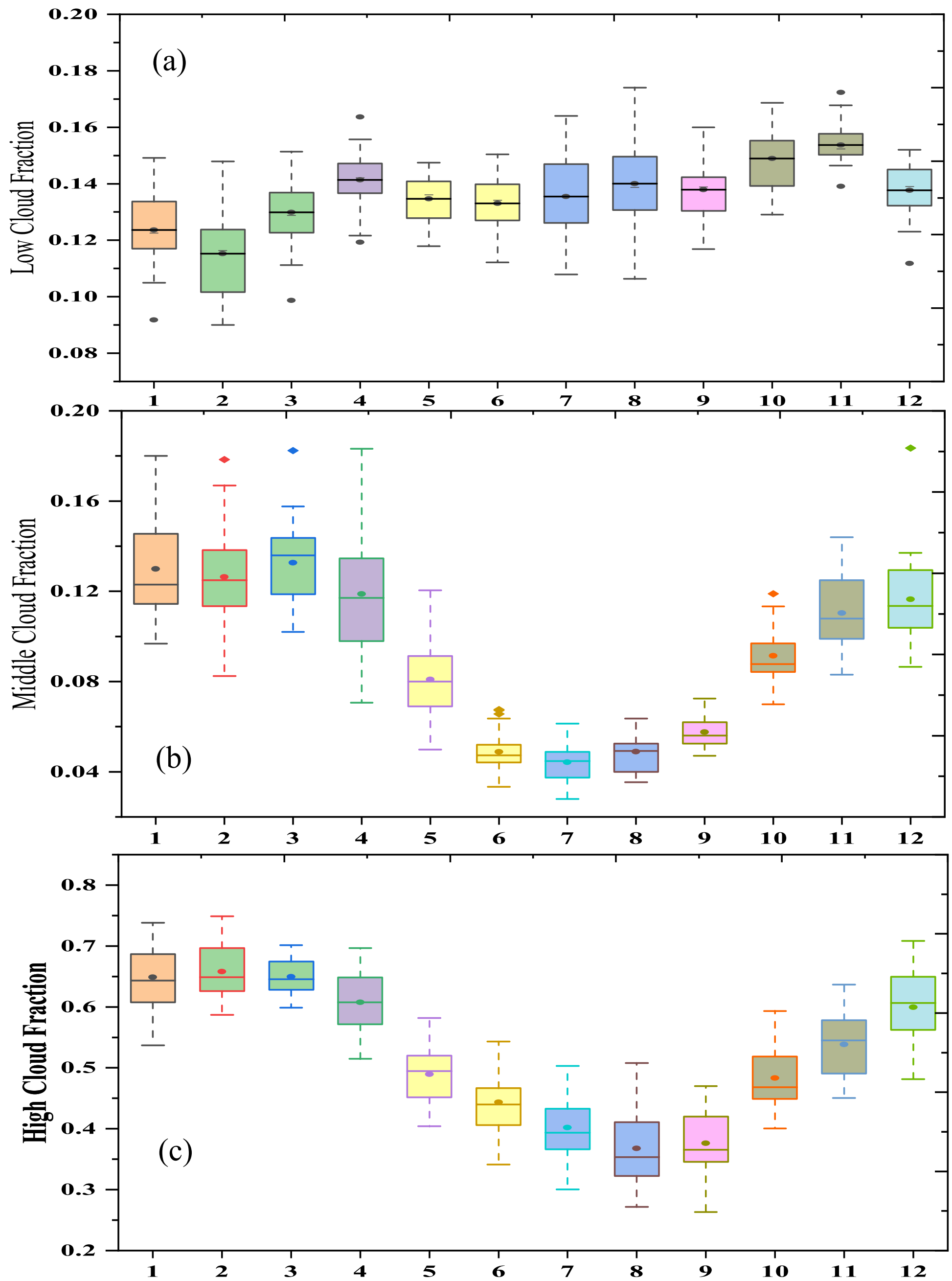

Fig. 6 Temporal variations of (**a**) low-level, (**b**) mid-level, and (**c**) high-level cloud area fraction over EA during the study period. The boxplots display the distribution of cloud area fraction values for each month. The central line indicates the median, the box edges show the interquartile range, and the mean values are represented by the dots within each box. Whiskers denote variability outside the upper and lower quartiles, while outliers are shown as individual points

development as the ITCZ migrates northward (Otte et al. 2023). In contrast, the lowest values occur during July and August, when the region experiences large-scale subsidence and dry conditions.

4.3 Spatiotemporal Trends of Cloud Area Fraction

The temporal trends in CAF over EA demonstrate marked variations across the low-, mid-, and high-level cloud layers, largely influenced by regional circulation systems, seasonal moisture dynamics and convective processes. This has been discussed in subsequent subsections.

4.3.1 Low-Level Cloud Area Fraction

The spatiotemporal trends in high-level CAF over East Africa, as depicted in Fig. 7; Table 1, exhibit a clear spatial variation in the regions of positive and negative trends. These trends reflect the complex interactions between large-scale circulation patterns, convective dynamics and surface climatic drivers. To start with, the trends are majorly positive and significant at 90% confidence level. Specific to note is that during JF, most of the study domain registered insignificantly low trends (between 0.001 and −0.001), probably due to the dry conditions experienced during this season.

Table 1 The monthly mean spatial distributions of low, mid, and high-level cloud area fractions, along with their temporal trends

Months	Mean spatial distributions of CAF			Temporal Trends of CAF		
	Low	Mid	High	Low	Mid	High
January	0.124 ± 0.013	0.130 ± 0.021	0.649 ± 0.052	0.0003 ± 0.0003	0.0005 ± 0.0006	0.0012 ± 0.0014
February	0.115 ± 0.015	0.126 ± 0.023	0.658 ± 0.044	0.0008 ± 0.0004	0.0003 ± 0.0005	0.0023 ± 0.0011
March	0.130 ± 0.012	0.133 ± 0.019	0.650 ± 0.030	0.0004 ± 0.0003	0.0002 ± 0.0005	0.0026 ± 0.0006
April	0.141 ± 0.010	0.119 ± 0.028	0.608 ± 0.050	0.0004 ± 0.0003	0.0023 ± 0.0006	0.0029 ± 0.0012
May	0.135 ± 0.008	0.081 ± 0.017	0.489 ± 0.045	0.0003 ± 0.0002	0.0006 ± 0.0004	0.0020 ± 0.0011
June	0.133 ± 0.009	0.049 ± 0.010	0.444 ± 0.054	0.0001 ± 0.0002	0.0002 ± 0.0003	0.0006 ± 0.0015
July	0.136 ± 0.015	0.044 ± 0.009	0.402 ± 0.053	0.0006 ± 0.0004	0.0004 ± 0.0002	0.0033 ± 0.0012
August	0.140 ± 0.017	0.049 ± 0.008	0.368 ± 0.065	0.0004 ± 0.0004	0.0001 ± 0.0002	0.0034 ± 0.0016
September	0.138 ± 0.011	0.058 ± 0.007	0.376 ± 0.054	0.0006 ± 0.0003	-0.0000 ± 0.0002	0.0030 ± 0.0014
October	0.149 ± 0.012	0.091 ± 0.012	0.483 ± 0.050	0.0005 ± 0.0003	0.0002 ± 0.0003	0.0018 ± 0.0014
November	0.154 ± 0.007	0.110 ± 0.018	0.539 ± 0.053	0.0003 ± 0.0002	0.0005 ± 0.0005	0.0019 ± 0.0014
December	0.138 ± 0.010	0.117 ± 0.020	0.600 ± 0.057	0.0002 ± 0.0003	-0.0009 ± 0.0005	-0.0006 ± 0.0016
Annual	0.136 ± 0.054	0.092 ± 0.035	0.522 ± 0.110	0.0003 ± 0.0001	0.0003 ± 0.0001	0.0021 ± 0.0006

However, the trends in the low-level CAF during JJA are significantly increasing (trend $> 0.002\ \text{year}^{-1}$) in most of the areas of the study domain, with the ITCZ having a great impact on the trends.

On the other hand, Table 1 shows a positive annual temporal trend in low-level CAF (0.0003 ± 0.0001), indicating a gradual but consistent increase in the extent of these clouds over time. This trend, although modest, is significant because it suggests that boundary-layer cloudiness could be responding to changes in near-surface temperature gradients and moisture recycling, potentially enhancing local cooling by increasing the reflection of incoming solar radiation. The highest positive trends occur in February (0.0008 ± 0.0004) and July (0.0006 ± 0.0004). This implies an intensification of low-cloud formation during transitional periods between dry and wet seasons, driven by rising surface temperatures and evolving regional circulation patterns.

4.3.2 Mid-Level Cloud Area Fraction

The spatial trends in mid-level clouds in Fig. 8 reveal strong regional variation across EA, with distinct zones of enhancement and suppression that shift throughout the year. The Northern parts of the domain exhibit a positive trend during the early months, indicating enhanced mid-tropospheric moisture and uplift. These trends are spatially coherent and align with regions influenced by the northward branch of the Hadley circulation and episodic deep convection. In contrast, equatorial and southern EA show widespread negative anomalies in the same period. This suggests that drier mid-tropospheric conditions and persistent subsidence over EA inhibit the formation of mid-level clouds.

As the year progresses, the spatial trends shift substantially, with positive trends emerging over equatorial and southern regions during the transition seasons. For instance, during boreal autumn, enhanced mid-level cloudiness appears across Tanzania and parts of coastal Kenya, consistent with the southward migration of the ITCZ and the onset of the short rains. The northern sector, conversely, transits into negative trends, indicating drying of the mid-troposphere and strengthened subsidence.

Table 1 shows the temporal trends in mid-level CAF over EA. Notably, the region exhibits clear spatial variations in positive and negative trends. These trends reflect the complex interactions between large-scale circulation patterns, convective dynamics, and surface climatic drivers. The overall temporal trend (0.0003 ± 0.0001) is weak but positive, indicating minimal long-term change in mid-level cloud extent. However, the strong positive trend in April (0.0023 ± 0.0006) is noteworthy; it signifies enhanced mid-tropospheric cloud formation during the peak of the long rains, driven by intensified convection and moisture convergence as the ITCZ moves northward.

4.3.3 High-Level Cloud Area Fraction

The spatiotemporal trends in high-level CAF over East Africa, as depicted in Fig. 9; Table 1, exhibit clear spatial patterns of positive and negative trends. Figure 9 shows widespread positive trends across much of the central, southern, and eastern parts of the study domain, with magnitudes generally ranging from 0.001 to 0.003. These increases are statistically significant at the 90% confidence level across most areas, suggesting a sustained rise in high-level cloud cover during the study period. The positive trends in high-level CAF could suggest intensified deep convection and enhanced upper-tropospheric moisture, likely associated with increased frequency and persistence of convective systems (Nicholson 2017; Otte et al. 2023). These changes could be attributed to the strengthening of the ITCZ and

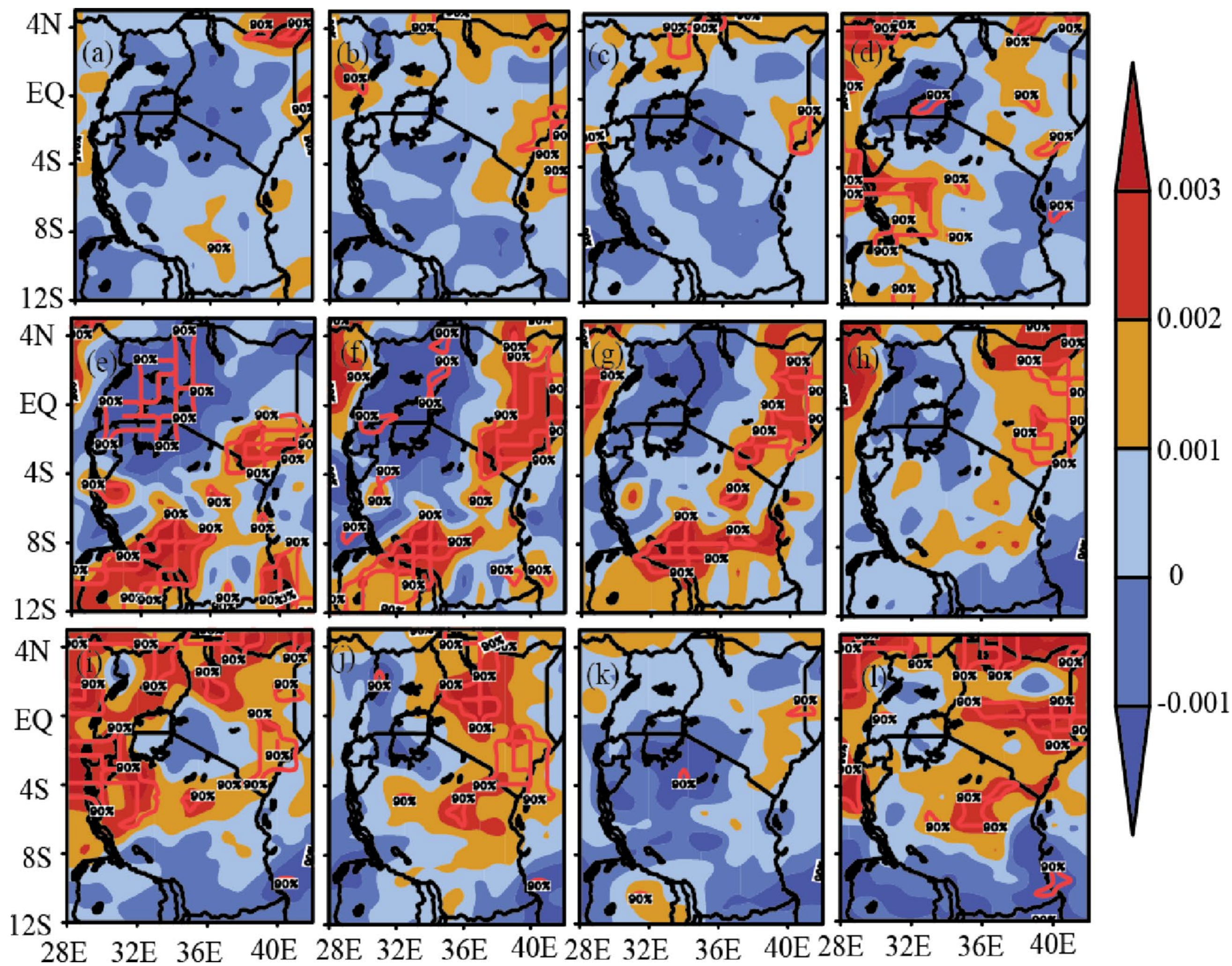

Fig. 7 Spatial distribution of trends in low-level CAF over EA for the period of study. The color bar indicates the magnitude and direction of the trends: positive values denote increasing trends, while negative values denote decreasing trends in CAF. Areas outlined with contours indicate regions where the trends are statistically significant at the 90% confidence level

greater surface evaporation driven by regional warming (Khamala et al. 2024). The enhanced presence of high clouds has a radiative role, reflecting a portion of incoming solar radiation while trapping outgoing longwave radiation, leading to a net positive radiative forcing that contributes to surface and atmospheric warming (Sassen and Wang 2012). Further, the positive trends could suggest a potential amplification of greenhouse effects in regions where high-level CAF has increased. This warming effect influences local and regional climate systems by altering precipitation intensity, delaying convective rainfall onset, and increasing surface temperatures (King et al. 2013; Khamala et al. 2024).

In contrast, the negative trends are observed mainly over the northern parts of the study domain, indicating a decline in high-level cloud cover in these regions. These negative trends imply weakening of deep convective activity, possibly linked to changes in the Walker circulation and reduced ITCZ penetration into northern latitudes during boreal summer (Williams and Funk 2011). The reduction in high-level clouds in these areas cools the surface by increasing longwave radiation escape to space, potentially leading to drier conditions.

From Table 1, it is evident that the annual mean temporal trend for high CAF is 0.0021 ± 0.0006. This is considered the strongest among all layers and is consistently highly positive across most of the months, particularly between March (0.0026 ± 0.0006) and September (0.0030 ± 0.0014). This persistent increase is significant because it points to intensifying upper-tropospheric convection and more frequent formation of high-level clouds. These significantly contribute to greenhouse warming by trapping outgoing longwave radiation, thereby influencing the regional energy balance and potentially amplifying climate feedback mechanisms.

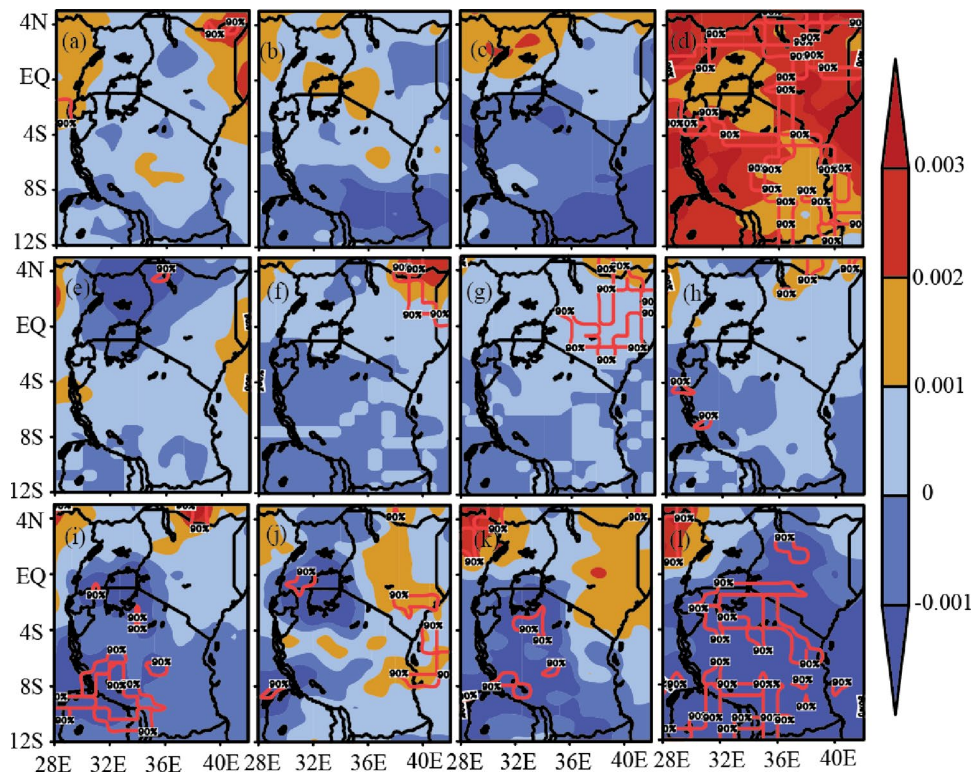

Fig. 8 Spatial distribution of trends in middle-level CAF over EA for the period of study. The color bar indicates the magnitude and direction of the trends: positive values denote increasing trends, while negative values represent decreasing trends in CAF. Areas outlined with contours indicate regions where the trends are statistically significant at the 90% confidence level

4.4 Cloud Radiative Effect (CRE)

Figure 10 illustrates the spatial distribution of CRE over the study domain. The results show significant regional variability, with positive values indicating net warming and negative values indicating net cooling. The spatial heterogeneity in CRE reflects the complex interplay between cloud properties and their radiative impacts on the surface and atmosphere. Notably, areas around the equator, especially around Lake Victoria, show pronounced positive CRE values ($10\ \mathrm{W\,m^{-2}}$). This implies enhanced longwave cloud radiative forcing associated with the trapping of outgoing longwave radiation, thereby contributing to warming. Conversely, most of the regions exhibit strongly negative CRE values between $-10\ \mathrm{W\,m^{-2}}$ and $-50\ \mathrm{W\,m^{-2}}$. These negative CRE zones suggest dominant shortwave cloud radiative effects, where cloud reflectivity reduces incoming solar radiation, thus exerting a cooling effect on the surface. The cooling effect modulates local surface temperatures and, in turn, indirectly affects regional atmospheric stability and moisture dynamics. As such, the contrast of positive and negative CRE values across EA underscores the significant spatial complexity of cloud-radiation interactions and their implications for regional climate processes.

Further, Table 2 shows temporal variability in CRE across EA. Notably, the CRE exhibits a distinct seasonal pattern driven by the interplay between SW cooling and LW warming processes. SW fluxes at the top of the atmosphere are strongly negative throughout the year, indicating substantial reflection of incoming solar radiation and thus a dominant cooling effect. This cooling is most pronounced during the MAM season, particularly in March (-70.68 $\mathrm{Wm^{-2}}$), when deep convective systems and extensive cloud cover are most developed (Nicholson 2017). Conversely, the LW component at the bottom of the atmosphere (BOA) remains positive throughout the year, reflecting the greenhouse-like warming effect of clouds. However, these LW values are consistently weaker than the SW cooling, resulting in an overall negative CRE across all months.

The seasonal transitions further modulate the magnitude of CRE. The smallest negative CRE values (-14.71 $\mathrm{Wm^{-2}}$; July) occur during the JJAS season, corresponding to the local dry season when cloud cover is minimal, and moisture availability is reduced (Anyah and Semazzi 2004). The annual mean CRE (-36.21 $\mathrm{Wm^{-2}}$) underscores the predominance of cloud-induced cooling over the region. This is consistent with climatological analyses indicating that tropical cloud systems exert strong net cooling due to their extensive coverage and high albedo (Nyasulu et al. 2020).

4.5 Cloud-Precipitation Interactions

The spatial distribution of CRE over EA reveals important links between cloud radiative impacts and regional precipitation patterns. Low clouds, which produce strongly negative shortwave CRE by reflecting incoming solar radiation.

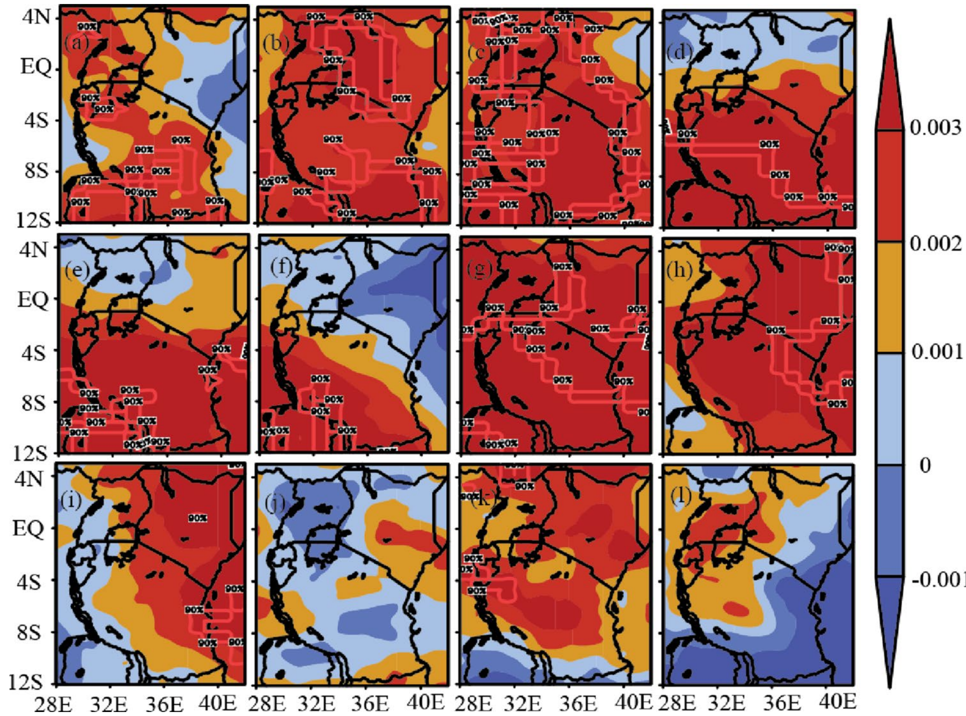

Fig. 9 Spatial distribution of trends in high-level CAF over EA for the period of study. The color bar indicates the magnitude and direction of the trends: positive values denote increasing CAF trends, while negative values denote decreasing CAF trends. Areas outlined with contours indicate regions where the trends are statistically significant at the 90% confidence level

This tends to reduce surface heating, thereby modulating the development of local convection. However, this cooling effect suppresses weak convective activity but also enhances moisture retention in the boundary layer, supporting light to moderate rainfall in certain regions. While the mid-level clouds exert a combination of shortwave cooling and longwave warming, influencing vertical moisture transport and the initiation of deeper convective systems. These clouds act as intermediaries, regulating moisture transport from surrounding areas and promoting rainfall as convective systems develop. High clouds, associated with strong positive longwave CRE, trap outgoing terrestrial radiation and warm the upper atmosphere, maintaining buoyancy in deep convective systems and often coinciding with regions of intense rainfall.

The net CRE, which integrates the shortwave and longwave contributions from all cloud layers, demonstrates clear spatial correspondence with observed precipitation patterns across the domain. Areas of positive net CRE generally align with zones of high convective activity and heavy rainfall, whereas regions dominated by negative net CRE are associated with reduced precipitation due to surface cooling and stabilized boundary layers.

The CRE-rainfall relationships are closely tied to the seasonal migration of the ITCZ, which drives strong upward motion, cloud formation, and intense precipitation near the equator. Regions under the ITCZ experience enhanced positive net CRE due to the dominance of high clouds, corresponding to deep convective rainfall, while regions outside the ITCZ show more negative net CRE, reflecting lower cloud coverage and reduced rainfall. By linking CRE patterns to the dynamics of the ITCZ, CRE not only shapes local energy balance but also reinforces the spatial and temporal patterns of rainfall across EA, providing a mechanistic explanation for observed precipitation variability as outlined by previous studies (Makokha et al. 2025).

5 Conclusions

The results of the present study are robust, though they are subject to limitations inherent in the MERRA-2 and CERES datasets, such as potential biases in cloud representation and temporal coverage, which should be considered when generalizing the findings. Thus, the spatiotemporal analysis of the vertical distribution of CAF and CRE from the MERRA-2 reanalysis modelled, and CERES observations in low, middle, and high clouds have exclusively been evaluated, and the following conclusions have been drawn from the findings:

1. The vertical, spatial, and temporal analyses of CAF reveal a strongly stratified cloud climatology over EA, shaped by the interplay of topography, lake-land interactions, and large-scale circulation systems such as the ITCZ and monsoonal flows. Low-level clouds (from surface to 680 hPa) that are $\sim$18% of the total CAF are modulated by boundary-layer thermodynamics and orographic uplift, while mid-level clouds (680–440 hPa) reflect sensitivity to moisture convergence and warming-induced

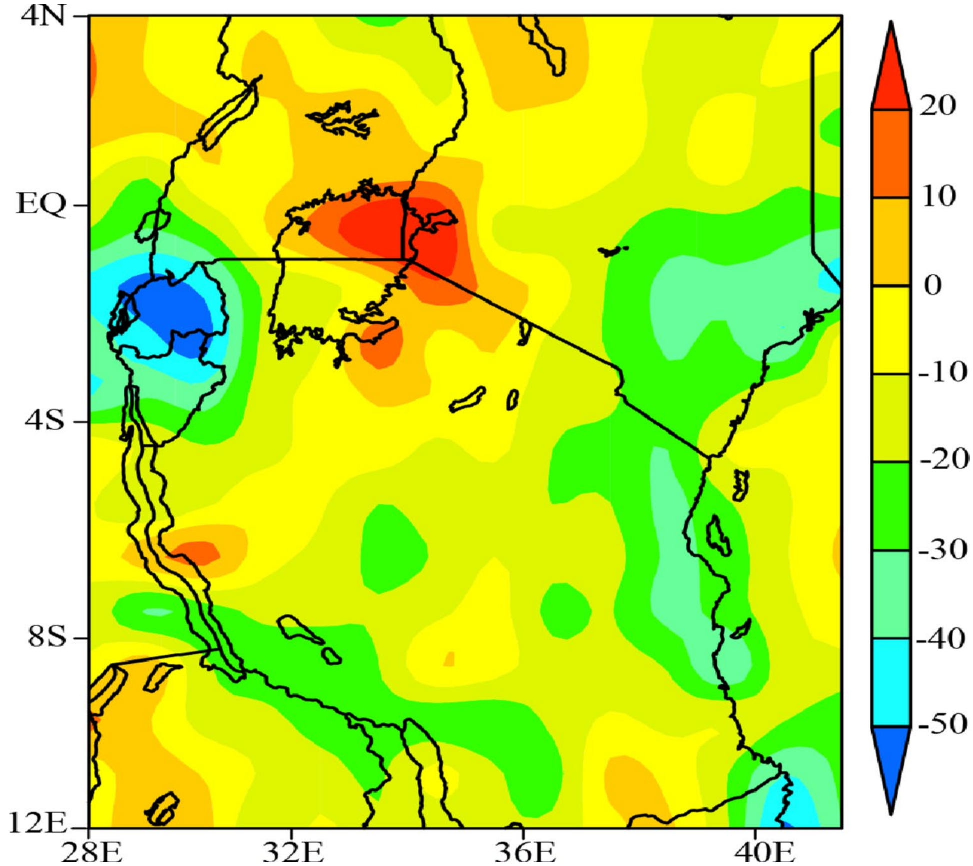

Fig. 10 Spatial distribution of CRE (Wm^{-2}) over EA. Positive values indicate areas where clouds contribute to net warming, while negative values indicate regions where clouds induce net cooling

Table 2 The monthly mean of cloud radiative effect (CRE in Wm^{-2}) using $CRE_{SW,TOA}$(in Wm^{-2}), $CRE_{LW,BOA}$(in Wm^{-2}) and their net (in Wm^{-2}) effect. The annual mean values confirm that shortwave cooling dominates over longwave warming, resulting in an overall cooling effect from clouds

Months	Cloud Radiative Effect		
	$CRE_{SW,TOA}$(A)	$CRE_{LW,BOA}$(B)	CRE (A+B)
January	-66.3092	11.9471	-54.3622
February	-64.4296	11.5282	-52.9014
March	-70.6762	12.1081	-58.5680
April	-60.9366	11.5896	-49.3470
May	-37.3335	9.8815	-27.4520
Jun	-24.4597	8.9103	-15.5494
July	-23.5835	8.8730	-14.7105
August	-25.9595	9.1823	-16.7772
September	-28.2743	9.3517	-18.9226
October	-41.8528	10.9515	-30.9013
November	-56.2596	11.7659	-44.4936
December	-62.0497	11.5142	-50.5355
Annual	-46.8437	10.6336	-36.2101

thermodynamic constraints. The high-level clouds (above 440 hPa) contribute to 60% of the total CAF trace deep convective cores tied to seasonal ITCZ migration. These patterns in the vertical CAF across the region reveal a complex, highly dynamic cloud-atmosphere coupling.

2. The trends reveal a systematic intensification of cloudiness across multiple layers, with the strongest increase occurring in high-level clouds. This is followed by moderate but positive trends in low- and mid-level clouds. These patterns reflect an evolving regional circulation, enhanced convection and increasing atmospheric moisture linked to ITCZ dynamics and regional warming.
3. The spatial and temporal patterns of CRE over East Africa reveal a dominant net cooling effect, primarily driven by a strong shortwave cloud radiative effect that

outweighs the warming influence of longwave processes. The annual mean CRE over the study domain is -36.21 W m^{-2}, highlighting the dominance of shortwave cooling. Whereas the regions near the equator, such as Lake Victoria, exhibit positive CRE values of $\sim$10 W m^{-2} due to longwave warming. Despite localized warming near equatorial regions such as Lake Victoria, most areas experience significant cooling due to high cloud reflectivity and extensive convective activity.

4. Cloud-precipitation interaction in the region is a vertically integrated process where each layer plays a distinct yet connected role in rainfall patterns. Low-level clouds trigger localized convection and seasonal rain onset; mid-level clouds regulate moisture transport and precede deep convection, and high-level clouds signal mature systems linked to heavy rainfall. Together, they reinforce the bimodal rainfall pattern by coordinating moisture, convection, and storm organization, underscoring the importance of cloud structure in the regional hydrological climate system.

Acknowledgements The authors gratefully acknowledge the use of NASA's Modern-Era Retrospective Analysis for Research and Applications, Version 2 (MERRA-2) data in this study. The high-quality reanalysis data provided by MERRA-2 were instrumental in analyzing cloud properties and radiative effects over the study region. The authors thank the Global Modelling and Assimilation Office (GMAO) for providing the MERRA-2 reanalysis data and the GES-DISC for disseminating MERRA-2 data. One of the authors (KRK) is grateful to the Department of Science and Technology (DST), Govt. of India, New Delhi, India, for awarding the DST-SERB-SRG (Grant No. SRG/2020/001445), DST-FIST Level 1 (Grant No. SR/FST/PS-1/2018/35), and DST-PURSE (SR/PURSE/2023/196) schemes to the Department of Physics, KLEF. The authors express their sincere gratitude to the German University of Technology in Oman (GUtech) for providing the financial support that enabled this research. The funding contributed to data acquisition, computational resources, and field validation activities essential to completing this study. The authors would like to acknowledge the Editor-in-Chief of the Journal and the four anonymous reviewers for their fruitful comments and constructive suggestions towards improving the earlier version of the manuscript.

Author Contributions All the authors have contributed to shaping ideas and revising the paper. *Geoffrey W. Khamala*: Conceptualization, Data Curation, Formal analysis, Methodology, Visualization, Investigation, Writing-Original draft preparation. *John W. Makokha*: Conceptualization, Methodology, Supervision, Writing-review and editing. *Churchill Wanyera*: Data Curation, Resources, Supervision, Writing-review and editing. *Kanike Raghavendra Kumar*: Data Curation, Methodology Validation, Supervision, Writing-review and editing. *Mansour Almazroui*: Data Curation, Validation, Writing-review and editing. *Pelati Althaf*: Data Curation, Visualization, Writing-review and editing. *Aqil Tariq*: Data Curation, Validation, Supervision, Writing-review and editing.

Funding This research did not receive any specific grant from funding agencies in the public, commercial, or non-profit sectors.

Data Availability Data will be made available upon reasonable request. However, the data that support the findings of this study are available openly and free to the public and can be downloaded at NASA/POWER Source Native, and https://gmao.gsfc.nasa.gov/reanalysis/MERRA-2/.

Code Availability Not Applicable.

Declarations

Consent for Publication All the authors agree to the publication of the present manuscript.

Ethical Approval All authors have read, understood, and complied as applicable with the statement on Ethical responsibilities of authors as found in the Instructions for Authors.

Competing Interests The authors declare that they have no known competing financial interests or personal relationships that could have appeared to influence the work reported in this paper.

Consent to Participate All the authors agree to the submission of this manuscript to the journal. The submitted work is original and has not been submitted/published elsewhere in any form or language (partially or in full).

Clinical trial Number Not Applicable.

References

B. Panet al. (2023) Baiwan Pan, Dantong Liu, Yuanmou Du, Delong Zhao, Kang Hu, Shuo Ding, Chenjie Yu, Ping Tian, Yangzhou Wu, Siyuan Li, KanikeRaghavendra Kumar. Intercomparisons on the Vertical Profiles of Cloud Microphysical Properties From CloudSat Retrievals Over the NorthChina Plain. Journal of Geophysical Research - Atmospheres, 128(13), e2023JD03909, 2023 https://doi.org/10.1029/2023JD039093

Baiwan Pan, Dantong Liu, Yuanmou Du, Delong Zhao, Kang Hu, Shuo Ding, Chenjie Yu, Ping Tian, Yangzhou Wu, Siyuan Li, KanikeRaghavendra Kumar. Intercomparisons on the vertical profiles of cloud microphysical properties from CloudSat retrievals over the North ChinaPlain. Journal of Geophysical Research: Atmospheres 128(13), 2023, e2023JD039093 https://doi.org/10.1029/2023JD039093

G Balakrishnaiah, B Suresh Kumar Reddy, K Rama Gopal, RR Reddy, LSS Reddy, C Swamulu, Y Nazeer Ahammed, K Narasimhulu, KKrishnaMoorthy, S Suresh Babu. Spatio-temporal variations in aerosol optical and cloud parameters over Southern India retrieved from MODISsatellite data. Atmospheric Environment 47, 435-445, 2012 https://doi.org/10.1016/j.atmosenv.2011.10.032

G Balakrishnaiah, K Raghavendra Kumar, B Suresh Kumar Reddy, C Swamulu, K Rama Gopal, RR Reddy, LSS Reddy, Y Nazeer Ahammed, KNarasimhulu, K KrishnaMoorthy, S Suresh Babu. Anthropogenic impact on the temporal variations of black carbon and surface aerosol massconcentrations at a tropical semi-arid station in southeastern region of India. Journal of Asian Earth Science 42(6), 1297-1308, 2011 https://doi.org/10.1016/j.jseaes.2011.07.016

Honglin Pan, Gang Ren, Minzhong Wang, Jin Wang, Kanike Raghavendra Kumar. Investigation on the spatiotemporal and verticalstructure of ice cloud and aerosol parameters from multi-source satellite datasets (2007–2021) over the Tarim Basin, China.

Journal ofAtmospheric and Solar-Terrestrial Physics 256, 106185, 2024a https://doi.org/10.1016/j.jastp.2024.106185

IPCC (2021) In: Masson-Delmotte, V., Zhai, P., Pirani, A., Connors, S.L., Péan, C., Berger, S., Caud, N., Chen, Y., Goldfarb, L., Gomis, M.I., Huang, M., Leitzell, K., Lonnoy, E., Matthews, J.B.R., Maycock, T.K., Waterfield, T., Yelekçi, O., Yu, R., Zhou, B. (Eds.), Climate Change 2021: The Physical Science Basis. Contribution of Working Group I to the Sixth Assessment Report of the Intergovernmental Panel on Climate Change. Cambridge University Press, Cambridge, United Kingdom and New York, NY, USA https://doi.org/10.1017/9781009157896

K Rama Gopal, G Balakrishnaiah, S Md Arafath, K Raja Obul Reddy, N Siva Kumar Reddy, S Pavan Kumari, K Raghavendra Kumar, TChakradhar Rao, T Lokeswara Reddy, RR Reddy, S Nazeer Hussain, M Vasudeva Reddy, S Suresh Babu, P Mallikarjuna Reddy. Measurements ofscattering and absorption properties of surface aerosols at a semi-arid site, Anantapur. Atmospheric Research, 183, 84-93,2017 https://doi.org/10.1016/j.atmosres.2016.08.016

Mangamana Aklesso, K Raghavendra Kumar, Lingbing Bu, Richard Boiyo. Analysis of spatial-temporal heterogeneity in remotely sensedaerosol properties observed during 2005–2015 over three countries along the Gulf of Guinea Coast in Southern West Africa. AtmosphericEnvironment 182, 313-324, 2018 https://doi.org/10.1016/j.atmosenv.2018.03.062

Althaf P, Kumar KR, Kannemadugu HBS (2024) Aerosol Optical Depth over the Andhra Pradesh State in South India from Reanalysis Data: Spatiotemporal Variabilities and Machine Learning Approach. Earth Syst Environ 9(4):2797–2821. https://doi.org/10.1007/s41748-024-00465-2

Anyah RO, Semazzi FHM (2004) Simulation of the East African climate using a regional climate model. Climate Res 25:145–160

Anyah RO, Semazzi FHM, Xie L (2006) Simulated physical mechanisms associated with climate variability over Lake Victoria Basin in East Africa. Mon Weather Rev 134(12):3588–3609. https://doi.org/10.1175/MWR3266.1

Ayugi BO, Wen W, Chepkemoi D (2016) Analysis of spatial and temporal patterns of rainfall variations over Kenya. J Environ Earth Sci ISSN ISSN2225-0948 (Online) 6(Paper):2224–3216

Matthews Nyasulu, Md Mozammel Haque, Richard Boiyo, Kanike Raghavendra Kumar, Yan-Lin Zhang. Seasonal climatology andrelationship between AOD and cloud properties inferred from the MODIS over Malawi, Southeast Africa. Atmospheric Pollution Reseach 11(11),1933-1952, 2020 https://doi.org/10.1016/j.apr.2020.07.023

Kang, N., Kumar, K.R., Yin, Y. et al. Correlation Analysis between AOD and Cloud Parameters to Study Their Relationship over China UsingMODIS Data (2003–2013): Impact on Cloud Formation and Climate Change. Aerosol Air Qual. Res. 15, 958–973 (2015) https://doi.org/10.4209/aaqr.2014.08.0168

Bhavyasree A, Reddy KRO, Balakrishnaiah G, Kotalo KRG, Thotli TLR, Virupakshappa UK, Rao TC, Lingala LSS, Narasimhulu K (2022) Measurements of aerosol optical depth and equivalent black carbon aerosols over a semi-arid region in southern India. Environ Dev Sustain. https://doi.org/10.1007/s10668-022-02380-w

Bhavyasree A, Tandule TCR, Balakrishnaiah G, Kalluri KRO, Thotli TLR, Gopal KR, Lingala SSR (2024) The effect of local pollution and transport dust on near surface aerosol properties over a semi-arid station from ground and satellite observations. Air Qual Atmos Health 17:541–558. https://doi.org/10.1007/s11869-023-01462-6

Black E, Slingo J, Sperber KR (2003) An observational study of the relationship between excessively strong short rains in coastal East Africa and Indian Ocean SST. Mon Weather Rev 131(1):74–94. https://doi.org/10.1175/15200493(2003)131%3C0074:AOSOTR%3E2.0.CO;2

Boiyo R, Kumar KR, Zhao T, Bao Y (2017) Climatological analysis of aerosol optical properties over East Africa observed from spaceborne sensors during 2001–2015. Atmos Environ 152:298–313. https://doi.org/10.1016/j.atmosenv.2016.12.050

Boiyo RK, Kumar R, Zhao T (2018) Spatial variations and trends in AOD climatology over East Africa during 2002–2016: a comparative study using three satellite data sets. Int J Climatol. https://doi.org/10.1002/joc.5446

Bosilovich MG, Robertson FR, Takacs L, Molod A, Mocko D (2015) MERRA-2: Initial evaluation of the climate. NASA Technical Report Series

Boucher O, Randall D, Artaxo P et al (2013) Clouds and Aerosols. IPCC AR5 Climate Change 2013. The Physical Science Basis

Camberlin P, Philippon N (2002) The East African March–May rainy season: Associated atmospheric dynamics and predictability over the 1968–97 period. J Clim 15(9):1002–1019. https://doi.org/10.1175/1520-0442(2002)015%3C1002:TEAMMR%3E2.0.CO;2

Caroline M, Wainwright AB, John H, Marsham C, David P, Rowell D, Declan L, Finney C, Black E (2021) Future changes in seasonality in East Africa from regional simulations with explicit and parameterized convection. Am Meteorol Soc. https://doi.org/10.1175/JCLI-D-20-0450.1

Dai A, Rasmussen KL, Liu C (2021) Variability and trends in tropical cloud systems and precipitation. J Clim 34(12):4899–4917. https://doi.org/10.1175/JCLI-D-20-0563.1

Dunning CM, Black ECL, Allan RP (2016) The onset and cessation of seasonal rainfall over Africa. J Geophys Research: Atmos 121(19):11405–11424. https://doi.org/10.1002/2016JD025428

Gebrechorkos SH, Hulsmann S, Bernhofer C (2019) Long-term trends in rainfall and temperature using high-resolution climate datasets in East Africa. Sci Rep 9:11376. https://doi.org/10.1038/s41598-019-47933-8

Gelaro R, McCarty W, Suarez MJ, Todling R (2017) The modern era retrospective analysis for research and applications, Version 2 (MERRA-2). J Clim 30(14). https://doi.org/10.1175/JCLID-16-0758.1

Giangrande SE, Collis SM, Theisen AK, Tokay A (2017) A summary of precipitation characteristics from MERRA-2. J Appl Meteorol Climatology 56(9):2547–2569

Hartmann DL, Ockert-Bell ME, Michelsen ML (1992) The effect of cloud type on Earth's energy balance: Global analysis. J Clim 5(11):1281–1304. https://doi.org/10.1175/1520-0442(1992)005

Hu K, Kumar KR, Kang N, Boiyo R, Jinwen and Wu (2018) Spatiotemporal characteristics of aerosols and their trends over mainland China with the recent Collection 6 MODIS and OMI satellite datasets. Environ Sci Pollut Res 25:6909–6927. https://doi.org/10.1007/s11356-017-0715-6

Althaf, P., Kumar, K.R., Kannemadugu, H.B.S. et al. Spatiotemporal Variability of Extinction Coefficient of Aerosols and Their Subtypes OverAndhra Pradesh, South India From the CALIPSO Data. Earth Syst Environ (2025) https://doi.org/10.1007/s41748-025-00936-0

Althaf, P., Kumar, K.R., Kannemadugu, H.B.S. et al. Spatiotemporal Variability of Extinction Coefficient of Aerosols and Their Subtypes OverAndhra Pradesh, South India From the CALIPSO Data. Earth Syst Environ (2025) https://doi.org/10.1007/s41748-025-00936-0

Khamala GW, Makokha JW (2025) Spatiotemporal Variability and Source Apportionment of Particulate Matter (PM) Emissions Using Binned Size Distributions: Insights from MERRA-2 over Africa. Earth Syst Environ. https://doi.org/10.1007/s41748-025-00641-y

Khamala GW, Makokha JW, Boiyo R, Kumar RK (2022) Long-term climatology and spatial trends of absorption, scattering and total aerosol optical depths over East Africa during 2001–2019. Environ Sci Pollut Res. https://doi.org/10.1007/s11356-022-20022-6

Khamala GW, Makokha JW, Boiyo R, Kumar KR (2023) Spatiotemporal analysis of absorbing aerosols and radiative forcing over environmentally distinct stations in East Africa during 2001–2018. Science of the Total Environment 864 (2023) 161041. https://doi.org/10.1016/j.scitotenv.2022.161041

Khamala GW, Makokha JW, Boiyo R (2024) The Spatiotemporal and dependency analysis of selected meteorological parameters and normalized difference vegetation index with aerosol optical depth over East Africa. https://doi.org/10.1016/j.heliyon.2024.e39961. Heliyon

Khan R, Kumar KR, Zhao T, Ullah W, de Leeuw G (2021) Interdecadal changes in aerosol optical depth over Pakistan based on the MERRA-2 reanalysis data during 1980–2018. Remote Sens 13:822. https://doi.org/10.3390/rs13040822

King MD, Menzel WP, Kaufman YJ, Tanré D, Gao B-C, Platnick S, Ackerman SA, Remer LA, Izenberg N, Martins JV (2013) Spatial and temporal distribution of clouds observed by MODIS. IEEE Trans Geosci Remote Sens 51(7):3826–3837. https://doi.org/10.1109/TGRS.2012.2227333

Balakrishnaiah, G., Raghavendra kumar, K., Suresh Kumar Reddy, B., Rama Gopal, K., Reddy, R. R., Reddy, L. S. S., Swamulu, C., Nazeer Ahammed, Y., Narasimhulu, K., KrishnaMoorthy, K., & Suresh Babu, S. (2012). Spatio-temporal variations in aerosol optical and cloud parameters over Southern India retrieved from MODIS satellite data. Atmospheric Environment (Oxford, England: 1994), 47, 435–445. https://doi.org/10.1016/j.atmosenv.2011.10.032 https://doi.org/10.1016/j.atmosenv.2011.10.032

Adesina, A.J., Kumar, K.R. & Sivakumar, V. Aerosol-Cloud-Precipitation Interactions over Major Cities in South Africa: Impact on RegionalEnvironment and Climate Change. Aerosol Air Qual. Res. 16, 195–211 (2016) https://doi.org/10.4209/aaqr.2015.03.0185

Kumar KR, Yin Y, Sivakumar V, Kang N, Yu X, Diao Y, Adesina AJ, Reddy RR (2015) Aerosol climatology and discrimination of aerosol types retrieved from MODIS, MISR and OMI over Durban (29.88∘S, 31.02∘E), South Africa. Atmos Environ 117:9–18. https://doi.org/10.1016/j.atmosenv.2016.12.050

Berhane, S. A., Kumar, K. R., & Bu, L. (2024). A 13-year space-based climatological evolution of desert dust aerosols in theMiddle East and North Africa regions observed by the CALIPSO. Science of The Total Environment, 948.

Liou KN (1986) Influence of cirrus clouds on weather and climate processes: A global perspective. Mon Weather Rev 114(6):1167–1199

Liu X, He T, Wang Q, Xiao X, Ma Y, Wang Y, Luo S, Du L, Wu Z (2025a) Estimation of long-term gridded cloud radiative kernel and radiative effects based on cloud fraction. Earth Syst Sci Data 17:2405–2428. https://doi.org/10.5194/essd-17-2405-2025

Liu X, He T, Wang Q, Xiao X, Ma Y, Wang Y, Luo S, Du L, Wu Z (2025b) Estimation of long-term gridded cloud radiative kernel and radiative effects based on cloud fraction. Earth Syst Sci Data 17:2405–2435. https://doi.org/10.5194/essd-17-2405-2025

Loeb NG et al (2018) Clouds and the Earth's Radiant Energy System (CERES) Energy Balanced and Filled (EBAF) dataset. J Clim 31(2):895–918

Lubis WS, Harrop EB, Lu J, Leung LR, Chen Z, Huang CS, Y, Omrani N (2025) Cloud radiative effects significantly increase wintertime atmospheric blocking in the Euro-Atlantic sector. Nat Commun 16:9763. https://doi.org/10.1038/s41467-025-64672-9

Makokha JW, Masayi NN, Barasa P, Ikoha AP, Konje MM, Mutonyi J, Okello VS, Wechuli AN, Majengo CO, Khamala GW (2024) Assessing the Long-Term changes in selected meteorological parameters over the North-Rift, Kenya: A regional climatology perspective. Hydrology 12(3):59–76. https://doi.org/10.11648/j.hyd.20241203.12

Makokha et al., 2025 John W Makokha, Peter W Barasa, Geoffrey W Khamala. Enhancing climate resilience: A data-driven north rift weather prediction system for real-time forecasting and agricultural decision support. Heliyon 11(4), e42549, 2025 https://doi.org/10.1016/j.heliyon.2025.e42549

Mendoza V, Pazos M, Garduño R, Mendoza B (2021) Thermodynamics of climate change between cloud cover, atmospheric temperature and humidity. Sci Rep 11., Article 21244. https://doi.org/10.1038/s41598-021-00555-5

Munday C, Washington R, Hart N (2021) African low-level jets and their importance for water vapor transport and rainfall. Geophys Res Lett 48. https://doi.org/10.1029/2020GL090999. e2020GL090999

Mutemi JN (2003) Climate anomalies over Eastern Africa associated with various ENSO evolution phases (PhD thesis). University of Nairobi Kenya

Nicholson SE (2017) Climate and climatic variability of rainfall over eastern Africa. Rev Geophys 55(3):590–635. https://doi.org/10.1002/2016RG000544

Nicholson SE (2018) The ITCZ and the seasonal cycle over equatorial Africa. Bull Am Meteorol Soc 99(2):337–348. https://doi.org/10.1175/BAMS-D-16-0287.1

Honglin Pan, Jianping Huang, Kanike Raghavendra Kumar, Linli An, Jinxia Zhang. The CALIPSO retrieved spatiotemporal and verticaldistributions of AOD and extinction coefficient for different aerosol types during 2007–2019: A recent perspective over global and regionalscales. Atmospheric Environment 274, 118986, 2022 https://doi.org/10.1016/j.atmosenv.2022.118986

Berhane, S.A., Althaf, P., Kumar, K.R. et al. A Comprehensive Analysis of AOD and its Species from Reanalysis Data over the Middle East andNorth Africa Regions: Evaluation of Model Performance Using Machine Learning Techniques. Earth Syst Environ 9, 3683–3708 (2025). S.A. Berhane, Kanike Raghavendra Kumar, Lingbing Bu. A 13-year space-based climatologicalevolution of desert dust aerosols in the Middle East and North Africa regions observed by the CALIPSO. Science of The Total Environment 948,174793, 2024 https://doi.org/10.1007/s41748-024-00513-x

Berhane, S.A., Althaf, P.,Kumar, K.R. et al. A Comprehensive Analysis of AOD and its Species from Reanalysis Data over the Middle East and North Africa Regions:Evaluation of Model Performance Using Machine Learning Techniques. Earth Syst Environ 9, 3683–3708 (2025) https://doi.org/10.1007/s41748-024-00513-x

Okoola RE (1996) Space-time characteristics of the ITCZ over Equatorial Eastern Africa during anomalous rainfall years (PhD thesis). University of Nairobi

Ongoma V, Chen H (2017) Temporal and spatial variability of temperature and precipitation over East Africa from 1951 to 2010. Meteorol Atmos Phys. https://doi.org/10.1007/s00703-016-04620

Otte T, Andersen H, Wood R (2023) Multi-layer cloud characteristics and radiative effects over the tropics. Atmos Chem Phys 23(9):5631–5649. https://doi.org/10.5194/acp-23-5631-2023

Ramanathan V, Cess RD, Harrison EF et al (1989) Cloud-radiative forcing and climate: Results from the Earth Radiation Budget Experiment. Science 243(4887):57–63

Reddy PSN, Tandule CR, Kalluri KRO, Gugamsetty G, Kotalo RG, Thotli LR, Akkiraju B, Lingala SSR (2021) The impact of lockdown on black carbon mass concentrations over a semi-arid region in Southern India: Ground observation and model simulations. Aerosol Air Qual Res 21(11) Article 210101. https://doi.org/10.4209/aaqr.210101

Rienecker MM, Suarez JM, Gelaro R, Todling R, Bacmeister J, Liu E, Bosilovich GM, Schubert DS, Takacs L, Kim G, Bloom S, Chen J, Collins D, Conaty A, Dasilva A, Gu W, Joiner J, Koster RD, Lucchesi R et al (2011) MERRA: NASA's modern-era retrospective analysis for research and applications. J Clim 24. https://doi.org/10.1175/JCLI-D-11-00015.1

Rossow WB, Schiffer RA (1999) Advances in understanding clouds from ISCCP. Bull Am Meteorol Soc 80(11):2261–2287

Sassen K, Wang Z (2012) The impact of thin cirrus clouds on climate: A global perspective. J Geophys Research: Atmos 117(D19):D19201. https://doi.org/10.1029/2012JD018094
Segele ZT, Leslie LM, Tarhule AA (2015) Sensitivity of Horn of Africa rainfall to regional sea surface temperature forcing. Climate 3(2):365–390. https://doi.org/10.3390/cli3020365
Simiyu KW, Khamala GW, Makokha JW (2025) Long-term characterisation of Dust and Its Radiative Forcing over Kenya Using Satellite and Model-Based Data. Atmospheric Clim Sci 15:723–741. https://doi.org/10.4236/acs.2025.154037
Stephens GL (2005) Cloud feedbacks in the climate system: A critical review. J Clim 18(2):237–273
Boucher, O. Randall, D. Artaxo, P. Bretherton, C. Feingold, G. Forster, P. Kerminen, V.-M. Kondo, Y. Liao, H. Lohmann, U. Rasch, P.Satheesh, S. K. Sherwood, S. Stevens, B. & Zhang, X. Y.* (2013). Clouds and aerosols. In T. F. Stocker, D. Qin, G.-K. Plattner, M. Tignor, S. K. Allen, J.Boschung, A. Nauels, Y. Xia, V. Bex, & P. M. Midgley (Eds.), Climate change 2013: The physical science basis. Contribution of Working Group I tothe Fifth Assessment Report of the Intergovernmental Panel on Climate Change (pp. 571–657). Cambridge University Press
Stubenrauch CJ et al (2013) Assessment of global cloud datasets from satellites: Project and database initiated by GEWEX radiation panel. Bull Am Meteorol Soc 94(7):1031–1049
Su X, Zhang Y, Li Z, Wang H (2025) Cloud–aerosol interactions and their radiative effects over Africa. Atmosphere 16(6):717
Sun J, Zhang K, Wan H, Ma P-L, Tang Q, Zhang S (2019) Impact of nudging strategy on the climate representativeness and hindcast skill of constrained EAMv1 simulations. J Adv Model Earth Syst 11:3911–3933. https://doi.org/10.1029/2019MS001831
Jing Huang, Lingbing Bu, Kanike Raghavendra Kumar, Rehana Khan, NSMP Latha Devi. Investigating the relationship between aerosoland cloud optical properties inferred from the MODIS sensor in recent decades over East China. 239, 117812,2020 https://doi.org/10.1016/j.atmosenv.2020.117812
Tierney JE, Ummenhofer CC, deMenocal PB (2015) Past and future rainfall in the Horn of Africa. Sci Adv 1(9):e1500682. https://doi.org/10.1126/sciadv.1500682
Vigaud N, Richard Y, Rouault M, Fauchereau N (2009) Moisture transport between the South Atlantic Ocean and southern Africa: Relationships with summer rainfall and associated dynamics. Clim Dyn 32(1):113–123. https://doi.org/10.1007/s00382-008-0377-7
Weatherhead EC, Reinsel GC, Tiao GC, Meng XL, Choi D et al (1998) Factors affecting the detection of trends: statistical considerations and applications to environmental data. J Geophys Res 103(D14):17149–17161. https://doi.org/10.1029/98JD00995
Wielicki BA, Barkstrom BR et al (1996) Clouds and the Earth's Radiant Energy System (CERES): An Earth observing system experiment. Bull Am Meteorol Soc 77(5):853–868
Williams AP, Funk C (2011) A westward extension of the warm pool leads to a westward extension of the Walker circulation, drying eastern Africa. Clim Dyn 37(11–12):2417–2435. https://doi.org/10.1007/s00382-010-0984-y
Williams AP, Seager R, Abatzoglou JT, Cook BI, Smerdon JE, Cook ER (2015) Contribution of anthropogenic warming to California drought during 2012–2014. Geophys Res Lett 42(16):6819–6828. https://doi.org/10.1002/2015GL064924
Winker DM et al (2010) The CALIPSO mission: A global 3D view of aerosols and clouds. Bull Am Meteorol Soc 91(9):1211–1229
Yang S, Xu B, Cao J, Zender CS, Wang M (2015) Climate Effect of Black Carbon Aerosol in a Tibetan Plateau Glacier. Atmos Environ 111:71–78. https://doi.org/10.1016/j.atmosenv.2015.03.016
Zelinka MD, Klein SA, Taylor KE, Andrews T, Webb MJ, Gregory JM, Forster PM (2013) Contributions of different cloud types to feedbacks and rapid adjustments in CMIP5. J Clim 26(14):5007–5027. https://doi.org/10.1175/JCLI-D-12-00555.1
Zelinka MD, Myers TA, McCoy DT, Po-Chedley S, Caldwell PM, Ceppi P, Klein SA, Taylor KE (2020) Causes of higher climate sensitivity in CMIP6 models. Geophys Res Lett 47(1) e2019GL085782. https://doi.org/10.1029/2019GL085782
Pan, H., Huang, J., Li, J., Huang, Z., Wang, M., Mamtimin, A., Huo, W., Yang, F., Zhou, T., and Kumar, K. R.: The Tibetan Plateau space-basedtropospheric aerosol climatology: 2007–2020, Earth Syst. Sci. Data, 16, 1185–1207, 2024 https://doi.org/10.5194/essd-16-1185-2024b